# A field-based thickness measurement dataset of fallout pyroclastic deposits in the peri-volcanic areas of Campania region (Italy): Statistical combination of different predictions for spatial thickness estimation

Pooria Ebrahimi[1,2], Fabio Matano[1], Vincenzo Amato[3], Raffaele Mattera[4], Germana Scepi[5]

[1] Institute of Marine Sciences (ISMAR), National Research Council (CNR), Naples, 80133 Italy
[2] Department of Earth, Environmental and Resources Sciences, University of Naples Federico II, Naples, 80126, Italy
[3] Department of Biosciences and Territory, University of Molise, Pesche (Isernia), 86090, Italy
[4] Department of Social and Economic Sciences, Sapienza University of Rome, Rome, 00185, Italy
[5] Department of Economics and Statistics, University of Naples Federico II, Naples, 80126, Italy

*Corresponding author*: Fabio Matano (fabio.matano@cnr.it)

**Abstract.** Determining spatial thickness (z) of fallout pyroclastic in-situ and reworked deposits plays a key role in volcanological studies and shedding light on geomorphological and hydrogeological processes in peri-volcanic areas. However, this is a challenging line of research because: (1) field-based measurements are expensive and time-consuming; (2) the ash might have been dispersed in the atmosphere by several volcanic eruptions; and (3) wind characteristics during an eruptive event and soil-forming/denudation processes after ash deposition on the ground surface affect the expected spatial distribution of these deposits. This article tries to bridge this knowledge gap by applying statistical techniques for making representative predictions of their spatial thickness finalized to the analysis of geomorphic processes at the catchment and sub-catchment scales. First, we compiled a field-based thickness measurement dataset (https://doi.org/10.5281/zenodo.8399487; Matano et al., 2023) of fallout pyroclastic deposits in the territories of several municipalities in Campania region, southern Italy. Second, 18 predictor variables were derived mainly from digital elevation models and satellite imageries and assigned to each measurement point. Third, the stepwise regression (STPW) model and random forest (RF) machine learning technique are used for thickness modelling. Fourth, the estimations are compared with those of three models that already exist in the literature. Finally, the statistical combination of different predictions is implemented to develop a less biased model for estimating pyroclastic thickness. The results show that prediction accuracy of RF (RMSE < 82.46 and MAE < 48.36) is better than that existing literature models. Moreover, statistical combination of the predictions obtained from the above-mentioned models through Least Absolute Deviation (LAD) combination approach leads to the most representative thickness estimation (MAE < 45.12) in the study area. The maps for the values estimated by RF and LAD (as the best single model and combination approach, respectively) illustrate that the spatial patterns did not alter significantly, but the estimations by LAD are smaller. This combined approach can help in estimating thickness of fallout pyroclastic deposits in other volcanic regions and in managing geohazards in areas covered with loose pyroclastic materials.

**Keywords**: fallout pyroclastic deposit thickness, random forest, stepwise regression, ensemble estimates, predictive modelling.

## 1. Introduction

A significant quantity of ash is dispersed in the atmosphere during an explosive volcanic eruption which deposits over a large area of ground surface following wind transportation. Spatial thickness of the ash layer typically decreases with distance from the eruptive vent (e.g., see Perrotta and Scarpati, 2003; Bourne et al., 2010; Lowe, 2011; Brown et al., 2012; Caron et al., 2012; Costa et al., 2012; Albert et al., 2019; Eychenne and Engwell, 2023) and noticeably influences geomorphological and hydrological processes such as landscape evolution, hillslope hydrology, erosion, and slope stability because the geotechnical and hydraulic properties of the unconsolidated ash layer usually differ from the underlying bedrock and soil. A deep understanding of the thickness of fallout pyroclastic deposits could, therefore, help address geohazard management and many related socioeconomic concerns. It is challenging to estimate the spatial thickness of fallout pyroclastic deposits because there might be more than one eruptive event, the ash-dispersal pattern is influenced by the changes in wind characteristics (e.g., the speed and direction of the wind) during a single eruption, and soil-forming and denudation processes continuously influence the expected spatial thickness due to different slope exposures and geometry. Only costly and time-consuming detailed field-based measurements may hallow to effectively map the thickness spatial variations of fallout pyroclastic deposits over a limited area (see for examples Matano et al., 2016, and Cuomo et al., 2021) The spatial thickness of fallout pyroclastic deposits under the influence of hillslope processes, accordingly, remained as a knowledge gap (De Vita et al., 2006a).

Estimating the residual regolith has been a common practice (e.g., Saulnier et al., 1997; Saco et al., 2006; Tesfa et al., 2009; Segoni et al., 2013) and the implemented models performed better when developed based on independent variables and applied to a specific site or in limited areas (Del Soldato et al., 2018; Matano et al., 2016). Conventional approaches for predicting pyroclastic thickness primarily rely on geological data, but the significant improvements in the availability of remote sensing data along with the recent advances in recording depositional history of fallout pyroclastic deposits present a unique opportunity to enhance prediction accuracy. Moreover, the statistical literature shows that better results can be achieved by combining estimations derived from different models, which has not been adopted for the objectives of this article to date.

This article explores the integration of a wide range of predictor variables, mainly derived from digital elevation model (DEM) and satellite multispectral images, and machine learning techniques (i.e. stepwise regression and random forest). These approaches identify the most relevant variables and capture non-linear relationships between the predictor variables and pyroclastic thickness values in order to improve prediction accuracy. Combination schemes were then applied to the predictions of these methods and those derived from classical approaches, namely Slope Angle Pyroclastic Thickness (SAPT; De Vita et al., 2006a), Geomorphological Pyroclastic Thickness (GPT; Del Soldato et al., 2016) and Slope Exponential Pyroclastic Thickness (SEPT; Del Soldato et al., 2018). Finally, the predictions are validated by field-based measurements of fallout pyroclastic deposits to empirically demonstrate that combining the results of different models provides better thickness predictions for the fallout pyroclastic deposits.

Different sections are briefly introduced here to provide a better insight into content of this article. Section 2 introduces the study area, while Section 3 explains data collection in the field along with the methodology for preparing the predictor variables and for predicting thickness of fallout pyroclastic deposits. In the next section, a detailed description of the field-based thickness measurement dataset and of the predictor variables is provided. Section 5 discusses the results and

highlights the advantages of using statistical combination in predicting thickness of fallout pyroclastic deposits. The concluding remarks and suggestions for future work are presented in the last section.

## 2. Study area

The area of interest encompasses Campania region and the immediate surroundings in south Italy (Fig. 1). It is bounded on the west by the Tyrrhenian Sea and on the east by the Apennine hilly-mountainous inner land with an altitude of up to 2050 m a.s.l. at Mt. Miletto. The area has a Mediterranean climate with hot, dry summers and moderately cool rainy winters. The mean annual temperature is about 10°C in the mountainous areas and roughly 18°C along the coast. The mean annual rainfall ranges from 700 mm in the eastern part of the region to 1800 mm in the central part of the Apennine mountains (Ducci and Tranfaglia, 2008).

The geological units of Apennine mountains are formed by Triassic to Early Miocene carbonate platform limestones and pelagic basin calcareous-pelitic sequences. They are strongly deformed, mainly thrusted eastward (Bonardi et al., 2009; Doglioni, 1991; Patacca et al., 1990) and uncomfortably covered by Middle Miocene to Pliocene thrust-top basin fillings, formed by siliciclastic sequences (mostly clay, sandstone, and conglomerate; Di Nocera et al., 2006).

The Quaternary extension in the hinterland and axial sectors of Campania region territory caused several fluvio-lacustrine intramontane basin openings (Ferranti et al., 2005; Amato et al., 2018; Boncio et al., 2022). The NW-SE and NE-SW striking faults delimit the strongly subsiding coastal basins (e.g., Volturno, Campania, Sarno and Sele plains) along the Tyrrhenian belt where the volcanic complexes of Somma-Vesuvius, Phlegrean Fields, Ischia and Roccamonfina occur (Fig. 1). The volcanoes are active (except for Roccamonfina) and erupted at least once in the last 1000 years (Rosi and Sbrana, 1987; Santacroce, 1987). Diffuse degassing, fumaroles and hot springs are observed around and in the submerged sectors of the volcanoes (Rosi and Sbrana, 1987; Chiodini et al., 2001; de Lorenzo et al., 2001). The above-mentioned volcanic complexes are briefly introduced below:

- The Somma-Vesuvius volcanic complex lies over a large sedimentary plain, prevalently filled by pyroclastic deposits. In this volcanic complex, the older Mt. Somma stratovolcano was cut by an eccentric polyphasic caldera and by the Vesuvius stratocone (Sbrana et al., 2020). Four main Plinian (Cioni et al., 2003; Santacroce et al., 2008; Sulpizio et al., 2010a,b; Mele et al., 2011; Sevink et al., 2011; Doronzo et al., 2022) and several interplinian eruptions (Andronico and Cioni, 2002; Cioni et al., 2015; Sulpizio et al., 2005, 2007; Bertagnini et al., 2006) have been linked to the volcanic activities of Somma-Vesuvius.

- The Phlegrean Fields consist of several volcanoes in a large caldera westward Naples, characterized by many eruptions with a large and very large Volcanic Explosivity Index (VEI; Newhall and Self, 1982) (Fig. 2). Volcanic activity in Phlegrean Fields began prior to 80 ka BP (Pappalardo et al., 1999; Scarpati et al., 2014) and the caldera collapses occurred during the eruptions of Campanian Ignimbrite (ca. 39 ka BP; Deino et al., 2004; De Vivo et al., 2001), Masseria del Monte Tuff (29 ka BP; Albert et al., 2019) and Neapolitan Yellow Tuff (15 ka BP; Orsi et al., 1996; Perrotta et al., 2006;Vitale and Isaia, 2014). The post-15ka activity was well described by Di Vito et al. (1999), Isaia et al. (2009) and Smith et al. (2011).

- Ischia Island is the emergent part of a volcanic edifice in the Gulf of Naples, whose activity started before 150 ka BP. The island is composed of volcanic rocks (mostly trachyte and phonolite) formed by effusive and explosive eruptions, epiclastic deposits and subordinate terrigenous sediments (De Vita et al., 2006b).

- The Roccamonfina volcanic complex was active between 550 and 150 ka BP in the Garigliano river rift valley. It was affected by an intense Plinian activity revealed by very large craters. The central caldera is the result of the eruptive explosions at 353±5 ka BP, while the latest stage of activity featured the edification of the central shoshonitic domes at 150 ka BP (Giannetti, 2001; Rouchon et al., 2008).

The fallout pyroclastic deposits considered in this article are mainly related to Somma-Vesuvius and Phlegrean Fields volcanoes (Fig. 2) because thickness of the Ischia tephra is not considerable on the mainland and the old Roccamonfina deposits have been mostly eroded outside the volcanic edifice. Therefore, only the volcanic history of Somma-Vesuvius and Phlegrean Fields will be further described in this section.
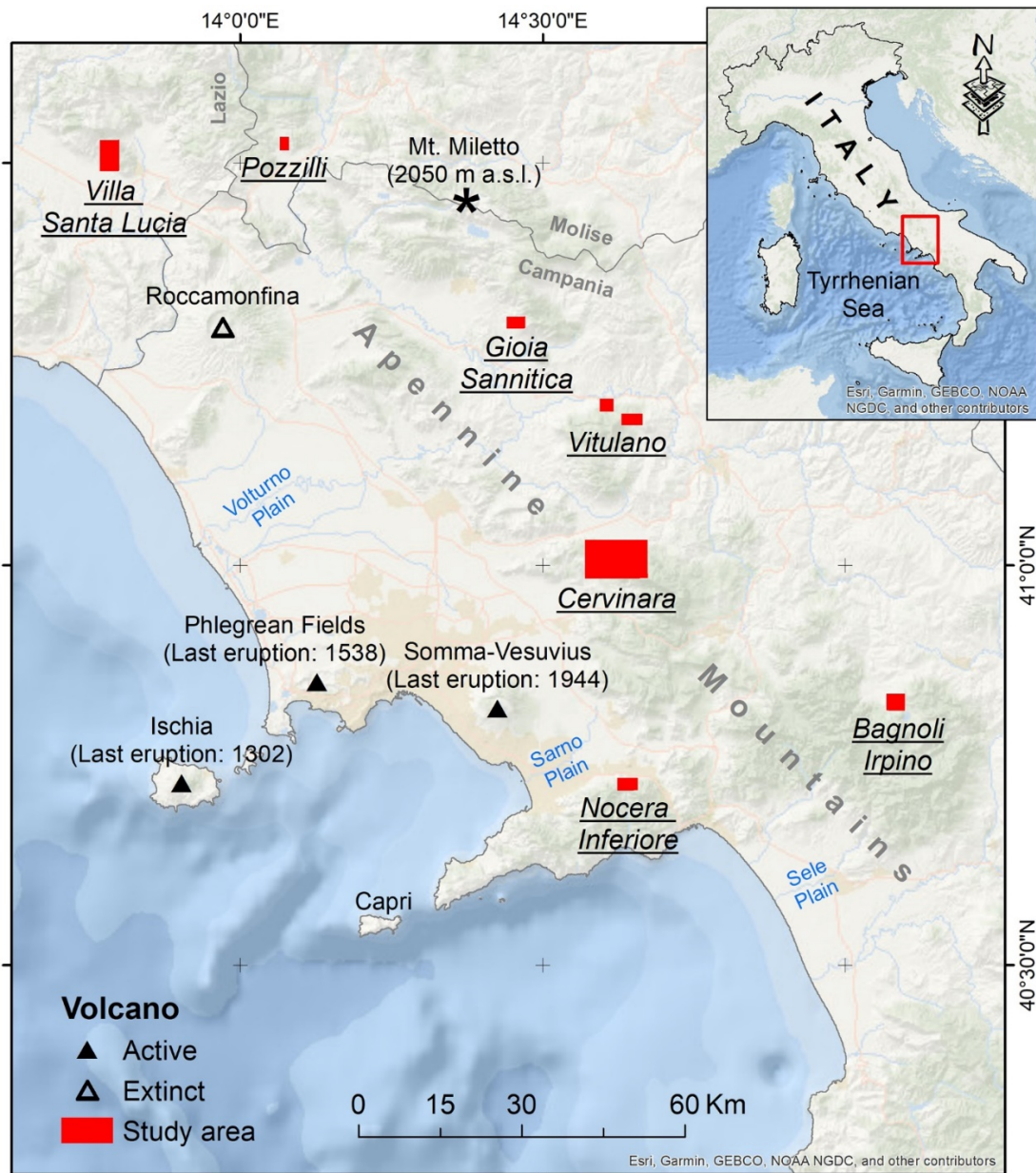
**Figure 1: Location of the study area in southern Italy.**

**2.1. The volcanic history of Phlegrean Fields**

The most important volcanic activities in Phlegrean Fields refer to the Campanian Ignimbrite (CI: 39 ka BP; De Vivo et al., 2001) and the Neapolitan Yellow Tuff eruptions (15 ka BP, Orsi et al., 1992, 1995; Wohletz et al., 1995; Deino et al., 2004). The former is the most powerful volcanic event ever occurred in the Mediterranean area (Barberi et al., 1978; Fisher et al., 1993; Orsi et al., 1996; Rosi et al., 1988, 1996; Civetta et al., 1997; De Vivo et al., 2001; Cappelletti et al., 2003; Engwell et al., 2014; Scarpati et al., 2015; Smith et al., 2016) that emplaced thick sequences of fallout deposits and pyroclastic density currents of mostly trachytic composition (Giaccio et al, 2008; Costa et al, 2022). The dispersed ash during the first eruptive phase was transported by wind toward east (Rosi et al., 1999; Perrotta and Scarpati, 2003; Scarpati and Perrotta, 2016). The pyroclastic density currents were subsequently emplaced over an area of 7,000 km$^2$ and surmounted ridges with more than 1,000 m high (Barberi et al., 1978; Fisher et al., 1993). The CI distal outcrops are mostly represented by a massive, grey ignimbrite (Barberi et al., 1978; Fisher et al., 1993; Scarpati et al., 2014), distributed beyond ~80 km from the vent (Smith et al., 2016).

The post-15ka activity of Phlegrean Fields was concentrated in three epochs separated by two quiescent periods (Fig. 2; Di Vito et al., 1999; Smith et al., 2011; Di Renzo et al., 2011 and references therein), and terminated with the Monte Nuovo eruption in 1538 CE (Guidoboni and Ciuccarelli, 2011; Di Vito et al., 2016 and references therein). The first epoch (15 to ~9.5 ka BP) is characterized by several explosive events, of which Pomici Principali eruption was the most energetic one (Lirer et al., 1987; Di Vito et al., 1999). This epoch was followed by a quiescent period when a thick paleosol layer, pedomarker A, was developed. The second epoch (8.6-8.2 ka BP; Di Vito et al., 1999) is distinguished by only a few episodes of low-magnitude eruptions mainly in NE Campanian Plain. After pedomarker B formation in a prolonged volcanic quiescence, the last epoch of intense volcanic activity began between 4.4 and 3.8 ka BP (Di Vito et al., 1999). The third epoch is characterized by several explosive events, of which the Agnano-Monte Spina eruption (4.4 ka BP; De Vita et al., 1999; Dellino et al., 2001) was the most powerful. This epoch was followed by a prolongate quiescent period and Monte Nuovo eruption (1538 CE; Di Vito et al., 1987; Piochi et al., 2005), respectively. Since 1960, fumarolic and hydrothermal activities with episodes of bradyseism mainly occur in Phlegrean Fields (Cannatelli et al., 2020).

## 2.2. The volcanic history of Somma-Vesuvius

The Somma-Vesuvius volcanic activity is characterized by four major Plinian eruptions (i.e. Pomici di Base or "Sarno" at ca. 22 ka BP, Mercato or "Ottaviano" at ca. 9.0 ka BP, Avellino at 3.9 ka BP and Pompeii at 79 CE) and several low-intensity interplinian eruptions (Fig. 2). Pomici di Base (Andronico et al., 1995; Santacroce et al., 2008) was the oldest caldera-forming event, which was followed by notably variable interplinian activities, alternating low-magnitude eccentric flank eruptions, quiescent phases and subplinian events (such as the Greenish Pumice eruption at ~19 ka BP; Santacroce and Sbrana, 2003; Santacroce et al., 2008). The products of Mercato eruption (Rolandi et al., 1993a; Mele et al., 2011) occurred about thirteen thousand years later were separated from those of Avellino eruption (Rolandi et al., 1993b; Sulpizio et al., 2010a,b; Sevink et al., 2011) by a thick paleosol layer (Di Vito et al., 1999). The low-intensity eruptions of AP1-AP6 (3.5-2.3 ka BP; Andronico et al., 2002; Santacroce et al., 2008; Passariello et al., 2010; Di Vito et al., 2019) preceded eruption of Pompeii which was well described by many authors (from Sigurdsoon et al. 1983 to Doronzo et al. 2023 and references therein).

The Vesuvius cone was formed by the most recent period of volcanic activity, characterized by a complex alternation of periods of activity with various explosive characters and quiescent phases (Andronico et al., 1995), suddenly interrupted by the Pollena eruption (472 CE; Rolandi et al., 2004). A Middle Age period of variable activity was then started, alternating lava effusions, moderately explosive eruptions, and mild periods (Rolandi et al., 1998), before a subplinian

eruption in 1631 CE (Bertagnini et al., 2006). After this event, the volcano entered a semipersistent mild activity with minor lava effusions and short quiescent periods. Each period of repose was preceded by relatively powerful explosive and effusive polyphase eruptions (Arrighi et al., 2001) like the last two ones in 1908 and 1944.
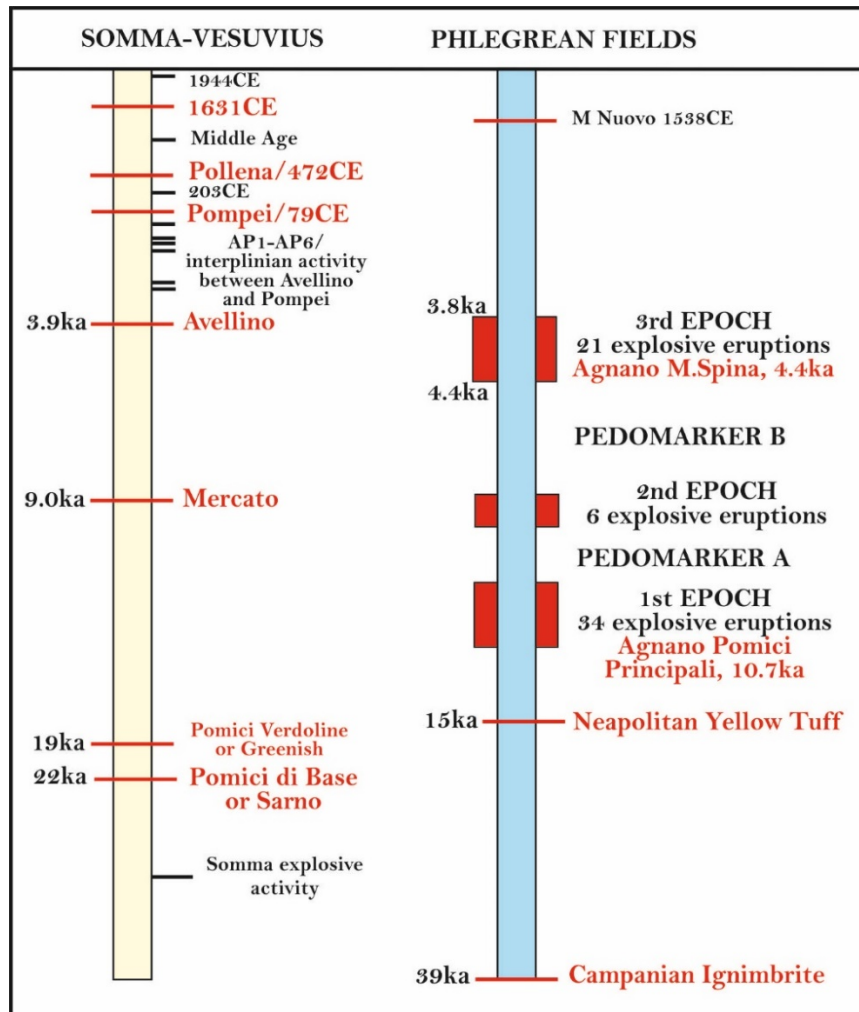
175

**Figure 2: Main explosive eruptions of Somma-Vesuvius and Phlegrean Fields volcanoes. The major explosive events are in red. The pedomarker A and pedomarker B refer to paleosol layers developed during eruptive quiescence.**

## 3. Materials and methods

The data and methods used in this study are summarized in Table 2 and Fig. 3 and further described in this section.

180
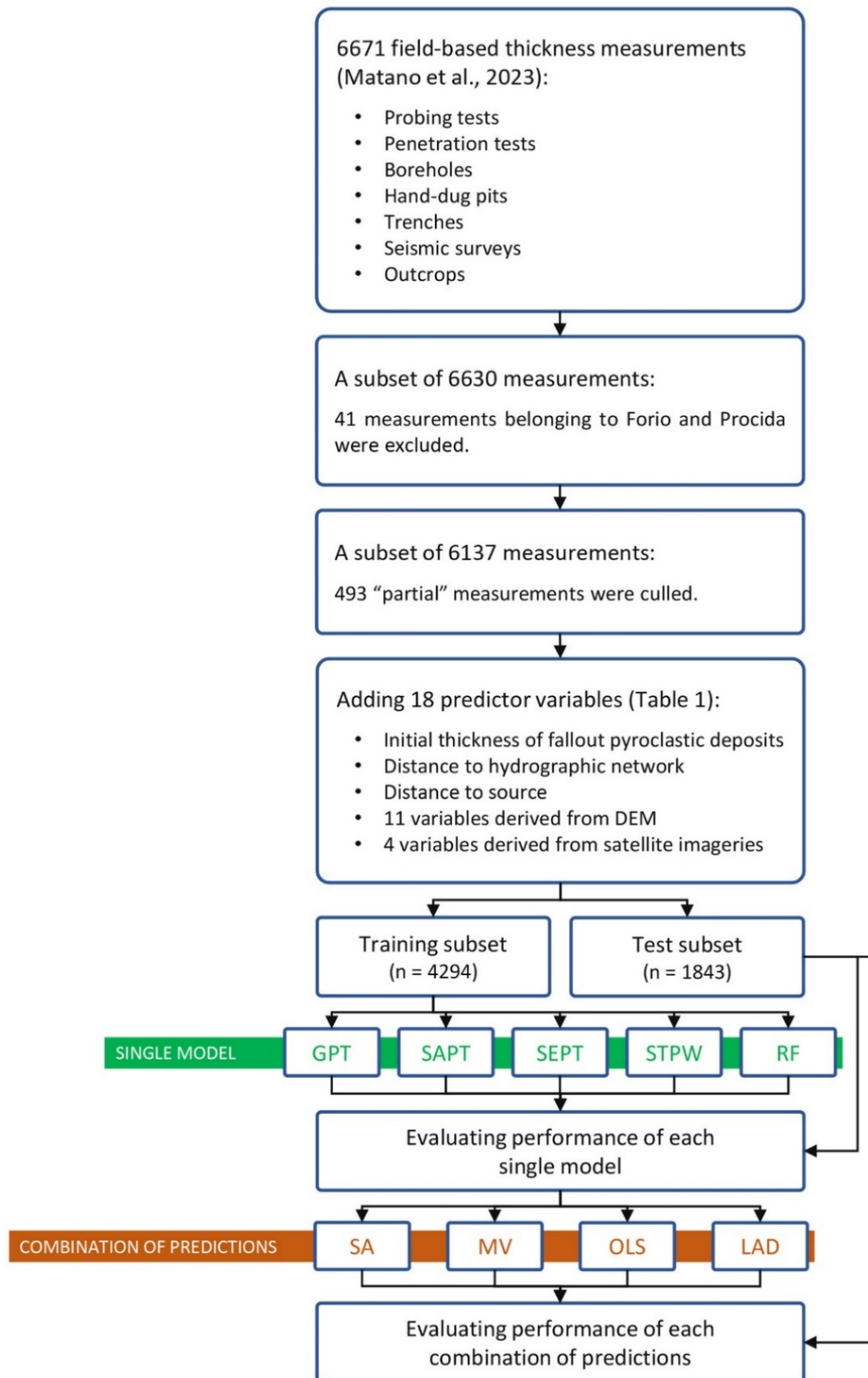
**Figure 3: A flowchart showing how the dataset of field-based thickness measurements (Matano et al., 2023) is used to predict thickness of the fallout pyroclastic deposits. GPT: Geomorphological Pyroclastic Thickness; SAPT: Slope Angle Pyroclastic Thickness, SEPT: Slope Exponential Pyroclastic Thickness; STPW: stepwise regression; RF: random forest; SA: Simple Average; MV: Minimum Variance; OLS: Ordinary Least Squares; LAD: Least Absolute Deviation.**

185

### 3.1. Dataset of field-based thickness measurements

A dataset of 6,671 field-based thickness measurements (Matano et al., 2023) has been collected during the field surveys and investigations for scientific and technical studies in the study area (Fig. 1) over the last decades. The measurements explain the distance between the topographic surface and the upper limit of the consolidated basement, referring to "total" measurement when the instrument could measure the whole distance and "partial" measurement when limitations of the implemented instrument led to measuring the distance partially. Further details about the stratigraphy of the pyroclastic deposits and the possible presence of non-lithified paleosols are not considered as they are beyond the scope of this article. The following methods have been applied for measuring thickness of the unconsolidated pyroclastic materials on the bedrock:

- Probing tests (PRBs): An iron rod (1.8 cm in diameter and up to 306 cm in length) was driven into the ground by hand or by a 0.03-kN hammer to measure depth of the underlying consolidated bedrock, indicating thickness of the fallout pyroclastic deposits as well. Each measurement represents the arithmetic mean of two or three measured values within a circle with a radius of 1-2 m to minimize the error associated with the local factors such as presence of cobbles, boulders, roots, colluvium and pumice layers.

- Penetration tests: Two types of penetration tests were implemented in this study. The Dynamic Cone Penetration tests (DPT–DL030) were performed by driving an iron rod with a cross-sectional area of 10 cm$^2$ into the ground by repeatedly raising a 0.3-kN weight for 20 cm and dropping it. It refers to the in-situ continuous measurement of rock/soil resistance to penetration up to 14 m depth which could also be an indirect measure for thickness of the fallout pyroclastic deposits when the probe fails to penetrate. The collected data by this method are in accordance with the probing test results and help interpret the stratigraphy as well. We also used the results of Standard Penetration Test (SPT), which is a common in-situ dynamic test for determining the geotechnical properties of subsurface soil such as relative density and shear strength parameters.

- Borehole (BH): The borehole stratigraphic data have been used for collecting thickness of fallout pyroclastic deposits.

- Hand-dug pits (HDPs): They were usually excavated manually (mainly 20×20×200 cm) near penetration test or geophysical survey sites for collecting further information on stratigraphy of the loose materials over the bedrock.

- Trenches (TRNs): They were excavated (1 m wide, 3 m long and 2-3 m deep) at the base of the slopes or along the intermediate morphological shelves using mechanical diggers for direct investigation of the pyroclastic deposit stratigraphy.

- Seismic surveys (SSs): Up to 10 m depth, the seismic reflection data of 3 bursts (direct, reverse and intermediate) were recorded by 20-24 geophones placed 3-5 m apart in a straight line on the ground surface. The seismic data revealed the geometry and stratigraphy of the ash layer along with the boundary between the consolidated bedrock and the overlaying loose materials.

- Outcrops (OCPs): Stratigraphy of several outcrops were analyzed across the study area for measuring thickness of the pyroclastic deposits.

For each method, the measurement error and estimated interpretation uncertainty (i.e. estimation of the fallout pyroclastic deposit thickness) are shown in Table 1. About 1 cm error is expected for direct thickness measurements through outcrops, hand-dug pits, trenches and boreholes. The error associated with the probing test results is around 1 cm as well. The measurement error of the penetration tests (i.e. Dynamic Cone Penetration test (DPT–DL030) and Standard Penetration Test) is considered 10 cm because the number of blows was counted following driving the rod into the ground for 10 cm.

In seismic surveys, the error depends on the specific technique and site characteristics, but a measurement error of 100 cm might be a good estimation for the whole study area.

The interpretative uncertainty of the measurements is equal to the measurement error (i.e. 1 cm) for direct thickness measurements, but increases in probing tests, penetration tests and seismic surveys. It is noteworthy that the results of these tests/surveys were calibrated in the field based on the more precise tests nearby (mostly at 1-10 m distance). The weighted average of errors and uncertainty are under 6 and 19 cm, respectively (Table 1). Therefore, the bias introduced by measurement errors and interpretative uncertainties is irrelevant to the objectives of this article.

| Measurement method | Numer of measurements | Percentage of measurements | Measurement error (cm) | Interpretation uncertainty (cm) |
|---|---|---|---|---|
| Borehole | 3 | 0.04 | 1 | 1 |
| Dynamic Cone Penetration test | 292 | 4.38 | 10 | 30 |
| Hand-dug pit | 317 | 4.75 | 1 | 1 |
| Outcrop | 152 | 2.28 | 1 | 1 |
| Probing test | 5373 | 80.54 | 1 | 10 |
| Seismic survey | 300 | 4.50 | 100 | 200 |
| Standard Penetration Test | 20 | 0.30 | 10 | 30 |
| Trench | 214 | 3.21 | 1 | 1 |
| Total | 6671 | 100 | | |
| Weighted average of errors | | | **5.9** | **18.6** |

Table 1: The expected measurement error and interpretation uncertainty for the methods implemented.

To date, partial/total thickness measurements, method of investigation, the municipality territory to which the measurement points belong, and the geographic coordinates are recorded in a total of 6,671 points (Matano et al., 2023). The spatial distribution of the measurement points is shown in Fig. 4. Matano et al. (2016) and Cuomo et al. (2021) have already used the measurements in Cervinara and Nocera Inferiore municipality territories for detailed thickness mapping with heuristic methods.
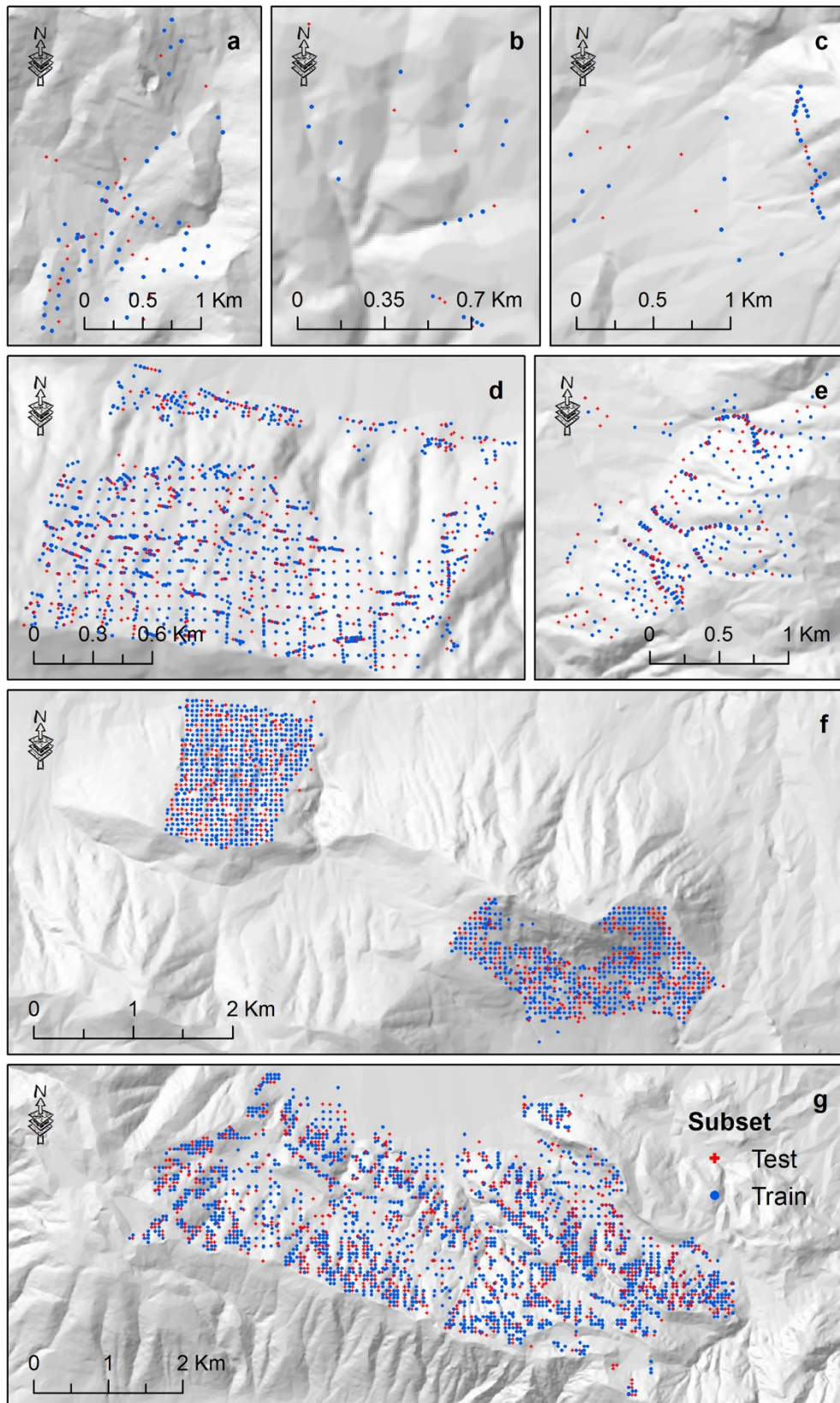
**Figure 4: Spatial distribution of field-based thickness measurement points in each municipality: (a) Villa Santa Lucia; (b) Pozzilli; (c) Gioia Sannitica; (d) Nocera Inferiore; (e) Bagnoli Irpino; (f) Vitulano; and (g) Cervinara. The measurement points are subdivided into the training (n = 4294) and test (n = 1843) subsets. Although symbols of different shapes and colours are used for the subsets, the spatially dense measurement points do not allow applying a larger symbol size. In the electronic version of this article, please zoom in on the figure to distinguish between different symbols based on the shape (if required).**

| Predictor variable | Description | Input data | Methodology | Tool |
|---|---|---|---|---|
| Altitude | It shows the elevation above sea level. | DEM [1] | N.A. [2] | N.A. |
| Aspect | It refers to the direction that the downhill slope faces. | DEM | Burrough and McDonell (1998); Ligas and Banasik (2011); Krakiwsky and Wells (1971); Lancaster and Salkauskas (1986); Hofmann-Wellenhof et al. (2001) | Aspect in ArcMap |
| Distance to hydrographic network | It indicates the distance to the hydrographic network. | ISPRA hydrographic network [3] | N.A. | Euclidean Distance in ArcMap |
| Distance to source | It represents the distance to the eruptive vents. | Di Vito et al. (2008) | N.A. | Euclidean Distance in ArcMap |
| Flow accumulation | Flow accumulation for a cell refers to the number of cells that flow to it. | DEM | Jenson and Domingue (1988); Tarboton et al. (1991) | Flow Accumulation in ArcMap |
| Flow direction | The flow direction for a cell indicates the direction water will flow out of the cell. | DEM | Greenlee (1987); Qin et al. (2007); Tarboton et al. (1991) | Flow Direction in ArcMap |
| Initial thickness ($z_0$) of fallout pyroclastic deposits | It refers to the thickness of fallout pyroclastic deposits that erupted from the volcanos without the influence of denudational processes. | See Tables S1 and S2 | See section 3.2.1 | ArcMap |
| Curvature | It is the second derivative of the surface, or the slope-of-the-slope. | DEM | Moore et al. (1991); Zevenbergen and Thorne (1987) | Curvature in ArcMap |
| Modified Secondary Soil-Adjusted Vegetation Index ($MSAVI_2$) | It indicates healthy green vegetation. | Landsat 8 OLI [4] | Qi et al. (1994) | Raster Calculator in ArcMap |
| Normalized Clay Index (NCI) | It is indicative of clay or hydroxyl-bearing minerals. | Landsat 8 OLI | Kienast-Brown et al. (2017) | Raster Calculator in ArcMap |
| Normalized Difference Vegetation Index (NDVI) | It shows healthy green vegetation. | Landsat 8 OLI | Jensen (2015) | Raster Calculator in ArcMap |
| Plan curvature | It is in the direction of the maximum slope. | DEM | Moore et al. (1991); Zevenbergen and Thorne (1987) | Curvature in ArcMap |
| Profile curvature | It is perpendicular to the direction of the maximum slope. | DEM | Moore et al. (1991); Zevenbergen and Thorne (1987) | Curvature in ArcMap |
| Slope | It identifies the steepness of the ground surface. | DEM | Burrough and McDonell (1998); Ligas and Banasik (2011); Hofmann-Wellenhof et al. (2001) | Slope in ArcMap |
| Stream power index (SPI) | It characterizes the erosive power of flowing water. | DEM | Moore et al. (1991) | Raster Calculator in ArcMap |

| Stream transport index (STI) | It shows the erosive power of surface flow. | DEM | Moore and Burch (1986) | Raster Calculator in ArcMap |
|---|---|---|---|---|
| Topographic wetness index (TWI) | It is a proxy for soil moisture. | DEM | Beven and Kirkby (1979); Moore et al. (1991) | Raster Calculator in ArcMap |
| Topsoil Grain Size Index (TGSI) | It represents the fine sand content of the topsoil. | Landsat 8 OLI | Xiao et al. (2006) | Raster Calculator in ArcMap |

[1] Vertical accuracy of the DEM is evaluated by control points and the overall root mean square error is <3.5 m (Tarquini et al., 2007); [2] Not applicable; [3] https://geodati.gov.it/resource/id/ispra_rm:01Idro250N_DT (accessed on 8 Jan. 2024); [4] Operational Land Imager. Landsat 8 OLI data are calibrated to better than 5% uncertainty in terms of Top of Atmosphere reflectance and have an absolute geodetic accuracy better than 65 m circular error at 90% confidence (Ihlen, 2019).

**Table 2: The predictor variables for thickness modeling.**

### 3.2. Predictor variables

A list of the potential predictor variables for estimating thickness of fallout pyroclastic deposits is provided in Table 2. The value for each predictor variable is assigned to the measurement points based on a set of rasters in 30×30 m resolution.

### 3.2.1. Initial thickness ($z_0$) of fallout pyroclastic deposits

This predictor variable represents the overall thickness of fallout pyroclastic deposits emplaced by Late Quaternary explosive eruptions at a given location. In other words, it explains the thickness value that could be estimated at a location if erosional and/or depositional processes do not occur after the associated eruptive events. In fact, the residual thickness of pyroclastic deposits that can be found at a certain location today is the result of the erosional and depositional processes that occurred after the eruptive events.

To obtain the initial thickness ($z_0$) of fallout pyroclastic deposits, the following approach is used: (1) collecting the isopach maps of the fallout deposits for the main volcanic eruptions (characterized by high explosivity index and great eruptive volume) in Campania region from literature (Tables S1 and S2); (2) georeferencing and digitizing each map; (3) applying an interpolation technique (i.e. Topo to Raster in ArcMap) to add intermediate isopaches in case of a significant gap between them; (4) assigning the average value of two isopaches of different thickness to the area between them, except for the area enclosed by only one isopach; (4) combining all shapefiles into one; (4) computing $z_0$ of all volcanic eruptions for each feature in the shapefile; and (5) converting the obtained shapefile into a raster with 30×30m resolution and assigning the $z_0$ value to each field-based measurement point in the thickness dataset (section 3.1).

The isopach maps of the fallout deposits for the Somma-Vesuvius and Phlegrean Fields main eruptions are listed in Tables S1 and S2, respectively. The Ischia tephra was not considered for $z_0$ calculation because of its insignificant thickness on the mainland. However, the old Roccamonfina tephra (>150 ka) has been almost entirely eroded outside the volcanic edifice and we have considered the associated isopach map of pyroclastic deposits only in a semi-quantitative way, based on the results of Rouchon et al. (2008) and Giannetti et al. (2001).

Isopach maps are commonly used in volcanological studies to estimate the volume of a single eruptive event and assess volcanic hazard. They are constructed by interpolating spatial thickness data points, considered reliable as directly measured by investigating the stratigraphy of volcanic deposits. To the best of our knowledge, uncertainty of the published isopach maps for Somma-Vesuvius and Phlegrean Fields (De Vita et al., 1999; Di Vito et al., 2008; Cappelletti et al.,

2003; Costa et al., 2009; Isaia et al., 2004; Orsi et al., 2004; Rolandi et al., 2003, 2004, 2007) has not been discussed in the literature. Only Costa et al. (2012) modeled the Campanian Ignimbrite isopach map based on 113 measurements and reported that the results are in agreement with the measured thickness values (relative mean error= ~0.3 log-units). The uncertainty is neither quantified for the cumulative isopach maps of multiple eruptions generated for studying erosional processes and landslide susceptibility (De Vita et al., 2006a; De Vita and Nappi, 2013; Del Soldato et al., 2016, 2018).

### 3.2.2. Variables derived from DEM and satellite imageries

The predictor variables from DEM or satellite imageries (11 and 4 variables, respectively) are listed in Table 2 with a definition, a brief description, and the methodology for obtaining them. Originally, the DEM is in 10×10m spatial resolution while the satellite imageries are in 30×30m spatial resolution. Raster resampling is, therefore, implemented after calculating the variables to obtain a resolution of 30×30m.

Other variables such as the distance to the hydrographic network and distance to the source (i.e. eruptive vent) are also considered as predictor variables in this study. In the latter, several inferred eruptive vents reported by Di Vito et al. (2008) along with Vesuvius crater and Roccamonfina caldera were considered to take into account different ash-producing eruptions and reduce the associated uncertainty as far as possible. Further information is provided in Table 2.

### 3.3. Methods for thickness modeling

### 3.3.1. Previous studies

To date, four approaches have been proposed for modeling thickness ($z$) of the fallout pyroclastic deposits. The Slope Angle Pyroclastic Thickness (SAPT) model estimates $z$ by linking the initial thickness ($z_0$) of fallout pyroclastic deposits erupted from the volcanos with the slope angle (De Vita et al., 2006a; De Vita and Nappi, 2013). In this model, some thresholds for slope angle were derived by field measurements in Mt. Sarno and Mt. Lattari. The Geomorphological Index Soil Thickness (GIST) model is an empirical model that combines morphometric, geomorphological and geological features (Catani et al., 2010) for estimating soil thickness in areas where bedrock weathering is the main soil forming process (Mercogliano et al., 2013; Segoni et al., 2013), but applied to the areas covered by the fallout pyroclastic deposits as well (Rossi et al., 2013). In this article, the GIST model was not implemented because the fallout pyroclastic deposits are of allochthonous origin and bedrock lithology does not control their thickness (De Vita et al., 2006a; Del Soldato et al., 2018). Del Soldato et al. (2016) proposed the Geomorphological Pyroclastic Thickness (GPT) model as a combination of the SAPT and GIST models. Comparing performance of GIST, SAPT and GPT models indicated that $z$ is mainly controlled by $z_0$ and slope gradient. Therefore, the Slope Exponential Pyroclastic Thickness (SEPT) model was developed based on these two parameters (Del Soldato et al., 2018).

### 3.3.2. Proposed methods: Random Forest

For spatial modeling, a wide range of machine learning techniques are available including logistic regression analysis, random forest (RF), support vector machine and artificial neural networks. Among these techniques, RF showed the best performance for classification and prediction. It is a shallow ensemble learning algorithm that could be tuned with few parameters (Liu et al., 2023 and references therein). The principles of decision trees and bagging are implemented for building random forests. Bagging applies bootstrap sampling of the training data for building decision trees and aggregates

the predictions across all the trees which reduces the overall variance and improves the predictive performance. The RF uses a random subset of variables at each split while growing a decision tree during the bagging process to generate a more diverse set of trees which helps lessen tree correlation beyond bagged trees and noticeably increase the predictive

325 power.

After splitting a given dataset randomly into training and test subsets (Fig. 4), the RF regression modeling could be applied as follows: (1) generating a RF model using the training subset; (2) calculating the variable importance for the established model; (3) applying the constructed RF model to the test subset and evaluating the results; and (4) implementing the trained RF model for making predictions in the unknown locations.

330 The R packages "rsample" (Frick et al., 2022) and "ranger" (Wright and Ziegler, 2017) are used for data splitting and modeling, respectively. We considered 70% of the whole dataset as training subset and the rest as test subset in data splitting (Fig. 4). For training a model, different values are assigned to each hyperparameter, including the number of variables to possibly split at each node ($m_{try}$), minimal node size to split at (*min.node.size*), sample with/without replacement (*replace*) and fraction of observations to sample (*sample.fraction*). A data frame from all possible

335 combinations of $m_{try}$, *min.node.size*, *replace* and *sample.fraction* was then generated, the RF model was trained for each combination and the best one was selected regarding root mean square error (RMSE) and mean absolute error (MAE) (see section 3.3.5 for more information). The optimum number of trees (*num.trees*) was finally investigated by running the RF model for 50 different *num.trees* values between 0 and 1000. Using the determined hyperparameters, the RF model is trained for making predictions, performance of the model is evaluated and the importance of variables is calculated by:

340 (1) the Gini index (Fig. 10b) which indicates the number of times a variable is responsible for a split and the impact of that split divided by the number of trees; and (2) the permutation importance (Fig. 10c) which calculates prediction accuracy in the out-of-bag observations and recomputes the prediction accuracy after eliminating any association between the variable of interest and the outcome by permuting the values of the variable under evaluation. The difference between the two accuracy values is the permutation importance for the given variable from a single tree. The average of importance

345 values for all trees in a RF then gives the RF permutation importance of this variable.

### 3.3.3. Proposed methods: Stepwise regression

Multiple linear regression is used to analyze the relationship between a single response variable (dependent variable) and two or more independent variables (predictor variables). Assuming we store $P$ predictor variables (p=1,…,P) for N

350 locations (i=1,…,N) in a matrix $X$ {$x_{i,p}$}, we could simply predict thickness $z$ {$z_i$} using multiple linear regression:

$$z = \beta X + \varepsilon \tag{1}$$

with $\beta = [\beta_1, …, \beta_P]'$ the vector of regression coefficients and $\varepsilon$ a vector of i.i.d. error terms. However, all the $P$ variables are not necessarily relevant for making prediction and more accurate predictions may be obtained by a subset $\widetilde{X}$ {$\tilde{x}_{i,p}, p = 1, …, \tilde{P}; \tilde{P} < P$} of predictor variables. Then, the final model can be written as follows:

355
$$z = \delta \widetilde{X} + \eta \tag{2}$$

with $\delta = [\delta_1, …, \delta_{\tilde{P}}]'$ the vector of the selected best $\tilde{P} < P$ variables and $\eta$ the new vector of error terms.

Different methods such as forward selection, backward elimination and stepwise regression (STPW) are used to this aim. All these methods are based on a series of automated steps (Taylor and Tibishirani, 2015). A forward-selection approach initially assumes no predictor variable and adds the most statistically significant variable, one by one, until no more

360 variable remains. On the contrary, the backward elimination approach initially includes all predictor variables and then eliminates the least statistically significant variables one by one. However, the STPW method is a combination of forward

selection and backward elimination. As with forward selection, the procedure starts with no variables and adds variables using a pre-specified criterion. At every step, the procedure also considers the statistical consequences of dropping the previously included variables. The STPW method is applied in this article with the R package "StepReg" (Li et al., 2020).

### 3.3.4. Proposed methods: Combination approaches

The RF, STPW, GPT, SAPT and SEPT models possess their own strengths and weaknesses. Previous studies showed that a combination of the predictions obtained with different methods allows for more accurate estimations (e.g., in the case of time series, see Eliott and Timmermann, 2004; Chan and Pauwels, 2016). Therefore, combination-based predictions are commonly used in many applicative fields (e.g., Cui et al., 2021; Nti et al., 2020; Wong et al., 2007; Yang, 2018).

One of the most common approaches for combining predictions is the stacking ensemble (Ganaie et al., 2022). It trains different models on the same dataset and generates predictions that become the input of a superior model (known as a second-level model; see Ribeiro, 2020). The fundamental concept behind stacking is that the optimal combination of the predictions of different models achieves better predictive performance compared to those obtained with single models.

Let us define, for each $i$-th location, a vector consisting of $K$ ($k = 1, \dots, K$) alternative predictive models $\hat{\mathbf{z}}_i = [\hat{z}_{i,1}, \hat{z}_{i,2}, \dots, \hat{z}_{i,k}, \dots, \hat{z}_{i,K}]'$ which can be obtained considering some inputs as shown in Fig. 4. Then, a final prediction at the $i$-th location can be defined according to:

$$\tilde{z}_i = f(\hat{\mathbf{z}}_i, \boldsymbol{\omega}) \tag{3}$$

with $\boldsymbol{\omega} = [\omega_1, \omega_2, \dots, \omega_k, \dots, \omega_K]'$ be the vector of $K$ weights associated with the $K$ different competing spatial predictive models. In other words, the stacking ensemble $\tilde{z}_i$ is a function of the $K$ predictions with different base models for the same location $\hat{\mathbf{z}}_i$. In particular, we assume a linear function:

$$\tilde{z}_i = \boldsymbol{\omega}'\hat{\mathbf{z}}_i = \sum_{k=1}^{K} \omega_k \hat{z}_{i,k} \tag{4}$$

In this framework, an important issue is the selection of the combination weights $\boldsymbol{\omega}$. To this aim, we can use subjective or objective weighting systems based on either expert evaluations or some statistical criteria. In this paper, we compare the performance of four objective weighting systems and choose the best one.

As the first approach, we consider the simple average (SA) combination in which the $K$ competing models are weighted equally, i.e. $\boldsymbol{\omega}_{SA} = [\frac{1}{K}, \dots, \frac{1}{K}]'$. Despite its simplicity, this approach empirically provides a better performance compared to more sophisticated alternatives (Hsiao and Wan, 2014). Another commonly adopted approach for optimal selection of combination weights is based on variance minimization criterion (MV, see Bates and Granger, 1969; Newbold and Granger, 1974). Given a set of $K$ competing predictive models, the weights are chosen by minimizing the variance of the prediction errors:

$$\min_{\boldsymbol{\omega}} \boldsymbol{\omega}'\boldsymbol{\Sigma}_{\mathbf{e}}\boldsymbol{\omega}, \qquad with \ \boldsymbol{\iota}'\boldsymbol{\omega} = 1 \tag{5}$$

with $\boldsymbol{\iota} = [1,1,\dots,1]'$ a vector of ones and $\boldsymbol{\Sigma}_{\mathbf{e}}$ the $K \times K$ covariance matrix associated to the prediction errors of the $K$ competing models. The optimal solution to this minimization problem is given by:

$$\boldsymbol{\omega}_{MV} = \frac{\boldsymbol{\Sigma}_e^{-1}\boldsymbol{\iota}}{\boldsymbol{\iota}'\boldsymbol{\Sigma}_e^{-1}\boldsymbol{\iota}} \tag{6}$$

where $\boldsymbol{\Sigma}_e^{-1}$ is the inverse of the covariance matrix, also known as the precision matrix.

The third approach implemented for choosing combination weights $\boldsymbol{\omega}$ is based on Ordinary Least Squares (OLS) regression (Granger and Ramanathan, 1984), where $\boldsymbol{\omega}$ can be chosen by considering the following linear regression:

$$z_i = \omega_0 + \sum_{k=1}^{K} \omega_k \hat{z}_{i,k} + \varepsilon_i \tag{7}$$

with $\omega_0$ the constant term, $\omega_k$ the generic k-th weight associated with the k-th competing model and $\varepsilon_i$ an i.i.d. error term. According to OLS combination, the weight vector $\boldsymbol{\omega} = [\omega_1, \dots, \omega_K]'$ is obtained by solving the following minimization problem:

$$\min_{\omega_1, \dots, \omega_K} \sum_{i=1}^{N} \left( z_i - \sum_{k=1}^{K} \omega_k \hat{z}_{i,k} \right)^2 \tag{8}$$

The OLS approach requires computing the weights in a training subset and using the selected ones in a test subset. It has the advantage of generating unbiased combined predictions without the need to investigate the bias for the individual models. This weighting approach is, however, sensitive to outliers. To address this issue, previous studies proposed the Least Absolute Deviation (LAD) combination approach, based on the minimization of the absolute loss function (Nowotarski et al., 2014):

$$\min_{\omega_1, \dots, \omega_K} \sum_{i=1}^{N} \left| z_i - \sum_{k=1}^{K} \omega_k \hat{z}_{i,k} \right| \tag{9}$$

### 3.3.5. Accuracy evaluation

To evaluate and compare performance of the $K$ predictive models and their combinations, Root Mean Square Error (RMSE) and the Mean Absolute Error (MAE) are computed. Let us first define the prediction error $e_{i,k}$ of the $k$-th model (including combinations of the models) for the observed $i$-th location:

$$e_{i,k} = z_i - \hat{z}_{i,k}.$$

The $RMSE_k$ and $MAE_k$ are defined as:

$$RMSE_k = \sqrt{\frac{1}{N} \sum_{i=1}^{N} e_{i,k}^2} = \sqrt{\frac{1}{N} \sum_{i=1}^{N} \left( z_i - \hat{z}_{i,k} \right)^2} \tag{10}$$

$$MAE_k = \sqrt{\frac{1}{N} \sum_{i=1}^{N} |e_{i,k}|} = \sqrt{\frac{1}{N} \sum_{i=1}^{N} |z_i - \hat{z}_{i,k}|} \tag{11}$$

Notice that MAE loss is less affected by outliers than RMSE and we prefer the models with lower MAE in case of ambiguity. The difference in accuracy of two competing models might also be due to randomness, especially for small differences. Therefore, several Equal Predictive Accuracy tests (EPA; Diebold and Mariano, 2002) were used in this article for comparing the $K$ competing models and their combinations and highlighting the statistically significant improvements in accuracy. Specifically, given two competing models $k$ and $k'$, we define a generic loss function $g(\cdot)$ of the prediction errors, $g(e_{i,k})$ and $g(e_{i,k'})$. In our case, we consider squared and absolute losses (RMSE and MAE, respectively). Let us define the loss differential vector $\boldsymbol{d} = [d_1, d_2, \dots, d_N]'$, where for each generic $i$-th location:

$$d_i = g(e_{i,k}) - g(e_{i,k'}) \tag{12}$$

430    Under the null hypothesis, the vector $d$ has zero mean and the two competing models $k$ and $k'$ have the same predictive accuracy. Under the alternative hypothesis, the two models are statistically different, and the best model is the one associated with the lowest statistical loss. In practice, the EPA test can be simply applied by regressing the loss differential vector $d$ with a constant vector $\iota$ of ones and by conducting inference with robust standard errors to account for possible heteroskedasticity.

435    **4. Description of the field-based thickness dataset and related predictor variables**

We first explain the process of creating a subset from the dataset of Matano et al. (2023) (n = 6671) to achieve our research objectives. Briefly, 41 measurements belonging to Forio and Procida municipalities are excluded because they are not located on the mainland. The subset is populated with 18 predictor variables and visualized in Figs. 5-8 to have an idea of the available data for detailed elaboration. It is noteworthy that the "partial" thickness measurements (n = 493) are then

440    culled, and the remaining 6137 points (Fig. 2) are considered for thickness modelling in the following section. The field-based thickness measurements range between 0 and 1450 cm. Most of the measurements refer to "total" thickness, representing thickness of fallout pyroclastic deposits from ground surface to the underlying bedrock (Fig. 5). The median of "partial" thickness values is three times greater than that of "total" thickness (approximately 200 and 60 cm, respectively). This is mainly due to applying the probing tests and the hand-dug pits in the areas with thick fallout

445    pyroclastic deposits, where thickness is greater than the maximum survey depth reached by these measurement methods, respectively 300 cm and 200 cm. The average and range of thickness values mainly show the limitations of the measurement methods. Probing test is the leading methodology implemented in field surveys and the measured values usually range from 10 to 300 cm. The recorded values are often <10 cm in outcrops and 200-800 cm in the measurements through SPT and boreholes. The greatest thickness in the dataset is determined by seismic surveys (Fig. 5d).

450    The surveys were mainly conducted in Cervinara, Nocera Inferiore and Vitulano territories (43, 24 and 24%, respectively; Fig. 5c). The median thickness values are above 60 cm in Nocera Inferiore and Cervinara while they fluctuate around 35 cm in the other municipalities (Fig. 5d). The values of predictor variables assigned to the "total" and "partial" measurement points are almost similar, but the minor differences have some interesting interpretations (Fig. 6). Compared to the stations for "total" measurements, the median values in Fig. 6 show that thickness is partially recorded in the

455    measurement points with lower altitude, distance to source and slope degree, but higher distance to hydrographic network (Fig. 6a, d, e and m). In addition, the distance of these stations to the hydrographic network is greater than that of "total" thickness measurement points (Fig. 6d). This last aspect confirms that the bedrock is usually not reached by investigation, and therefore the thickness is greater, as one moves away from the hydrographic network, the torrential erosive intensity being lower. The similarity between Fig. 5d (i.e. the three boxplots on the left) and 6r probably reveals that $z_0$ is a good

460    indicator of z.

The measurement points are also categorized regarding the measurement methods (Fig. 7) to underline the category-based variation of the predictor variables. The insignificant variation of the variables for the stations investigated through borehole stratigraphic data explains the few field-based observations under this category. Standard Penetration Tests and seismic surveys are the preferred methods in the low-altitude locations far from the hydrographic network and near the

465    source (Fig. 7a, d and e). On the contrary, thickness of the fallout pyroclastic deposits is investigated via trenches and outcrops in the measurement points farthest from the source (Fig. 7e). The lowest computed $z_0$ values are related to these stations as well (Fig. 7r). Curvature, plan curvature, profile curve and TWI show very similar distributions regardless of the methodology (Fig. 7c, k, l and q).

Likewise Fig. 7, range of the predictor values are compared in different municipalities (Fig. 8). It provides some spatial
information on each municipality and the measurement points belonging to them. For instance, Bagnoli Irpino and Villa
Santa Lucia occur at the highest and lowest altitudes, respectively (Fig. 8a). The latter has the lowest distance to the
hydrographic network along with the minimum calculated $z_0$ and measured $z$ values (Fig. 8d, 8r and 5d, respectively).
Cervinara and Nocera Inferiore are the closest municipalities to the source (Fig. 8e), where the greatest $z_0$ values are
calculated (Fig. 8r), above 65% of the measurements are performed (Fig. 5c), and the highest $z$ values are recorded (the
right panel of Fig. 5d). Taking into account Figs. 1 and 8r, significantly higher fallout pyroclastic deposits were emplaced
by volcanic activities in the eastern sector of the study area. The discussion in this section indicates a relatively high level
of heterogeneity of the variables. The presence of many data outliers can also be visually verified in Figs. 5-8. These
characteristics of the data suggest a complex relationship between the predictor variables and thickness of fallout
pyroclastic deposits, which can be better modeled by means of machine learning techniques rather than the standard
models employed in the literature.
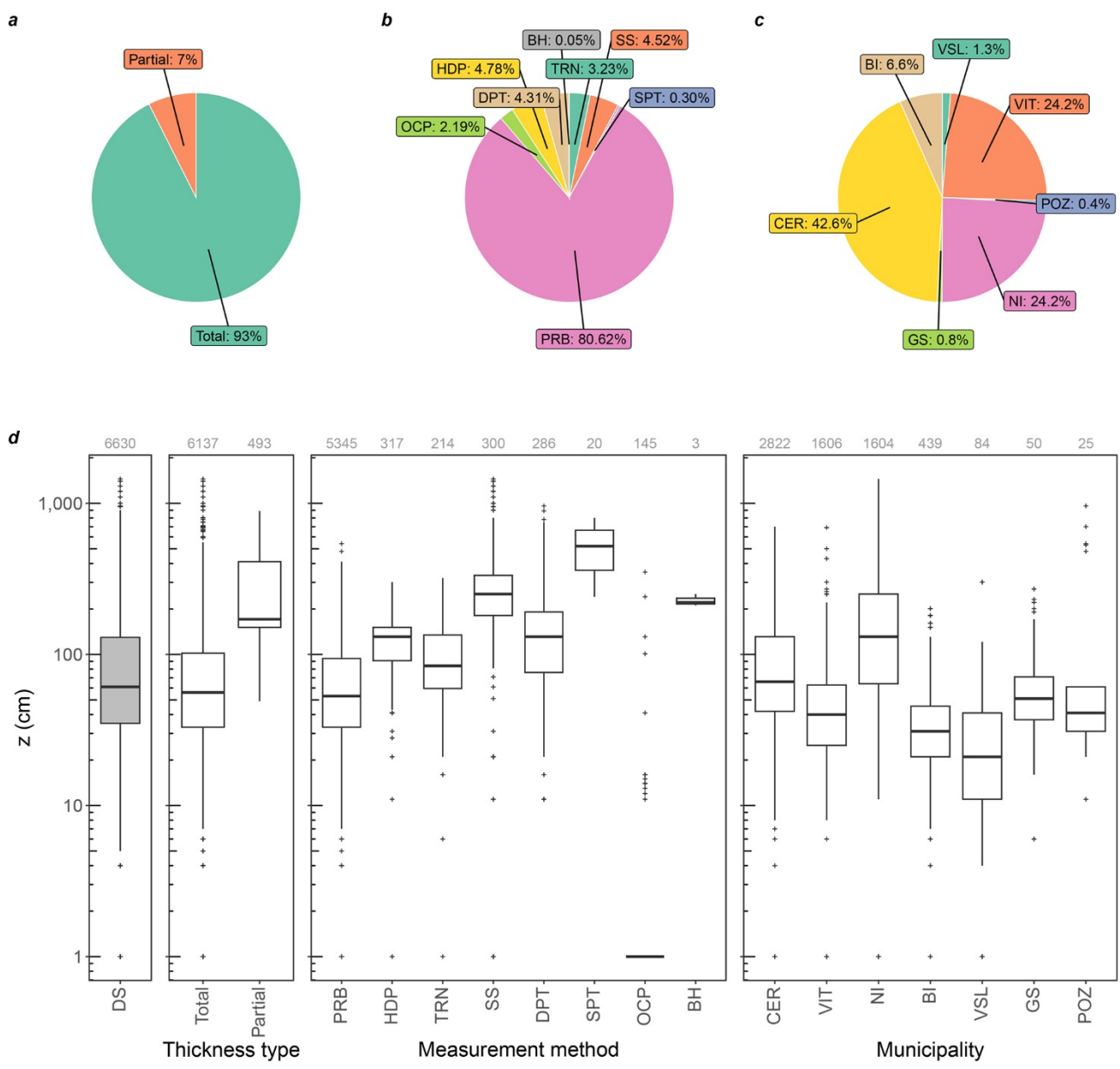
**Figure 5: An overview of the field-based thickness measurements of the fallout pyroclastic deposit in study area: (a) proportion of total and partial measurements; (b) proportion of the measurements regarding the methodology; (c) proportion of the measurements in each municipality; and (d) variation of thickness considering the whole dataset, total/partial measurements,**

485   **measurement method and municipality. DS: dataset; OCP: outcrop; PRB: probing test; TRN: trench; HDP: hand-dug pit; DPT: Dynamic Cone Penetration tests; BH: borehole; SS: seismic survey; SPT: Standard Penetration Test; NI: Nocera Inferiore; BI: Bagnoli Irpino; CER: Cervinara; VIT: Vitulano; GS: Gioia Sannitica; POZ: Pozzilli; and VSL: Villa Santa Lucia. It is noteworthy that the "partial" measurements are excluded for modelling thickness in this study.**
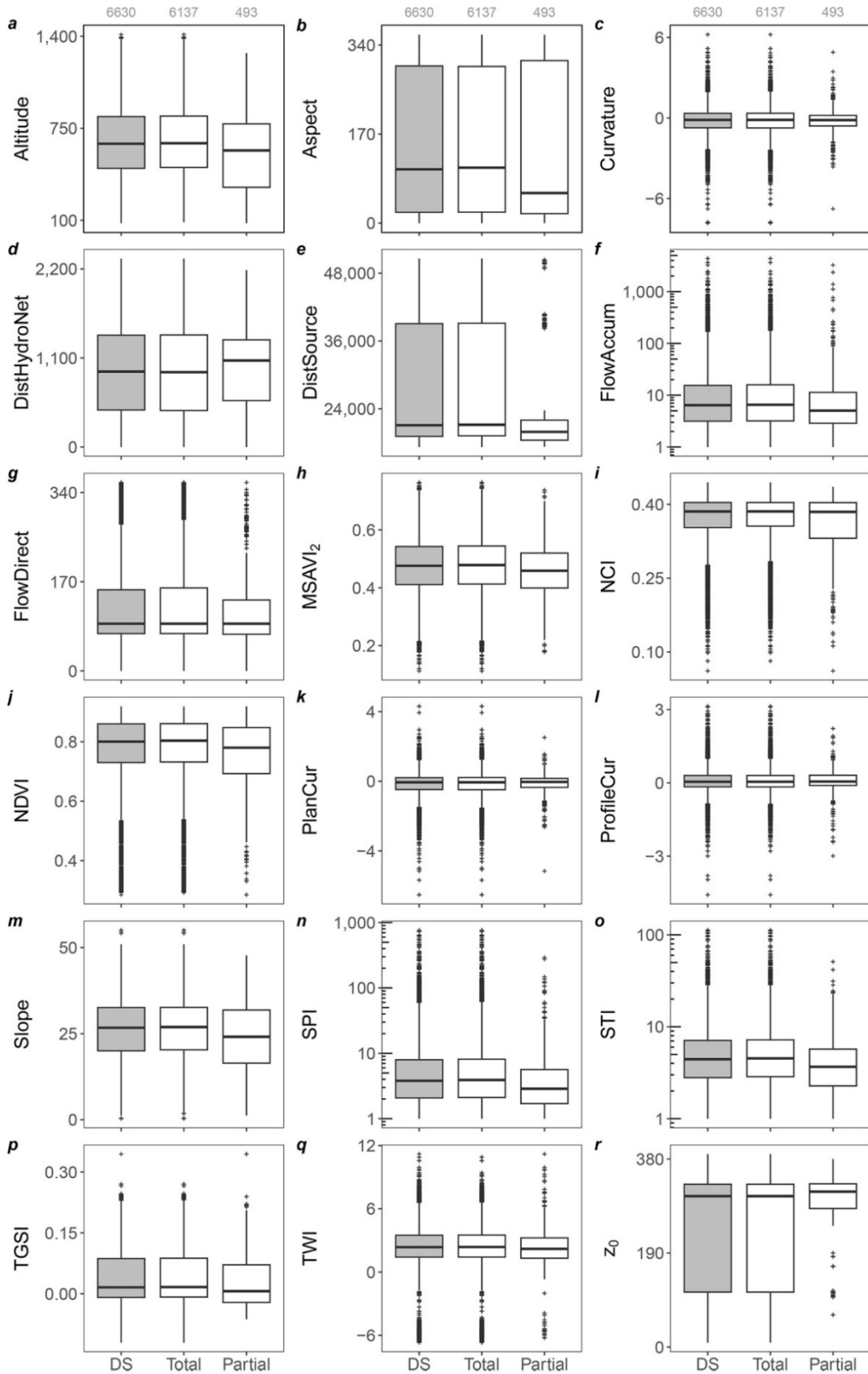
490   **Figure 6: Range of the values for predictor variables referred to the whole dataset (DS) and to the total/partial measurements. DistHydroNet: Distance to hydrographic network; DistSource: Distance to source; FlowAccum: Flow accumulation;**

**FlowDirect: Flow direction; PlanCur: Plan curvature; ProfileCur: Profile curvature. It is noteworthy that the "partial" measurements are excluded before thickness modelling in this study.**
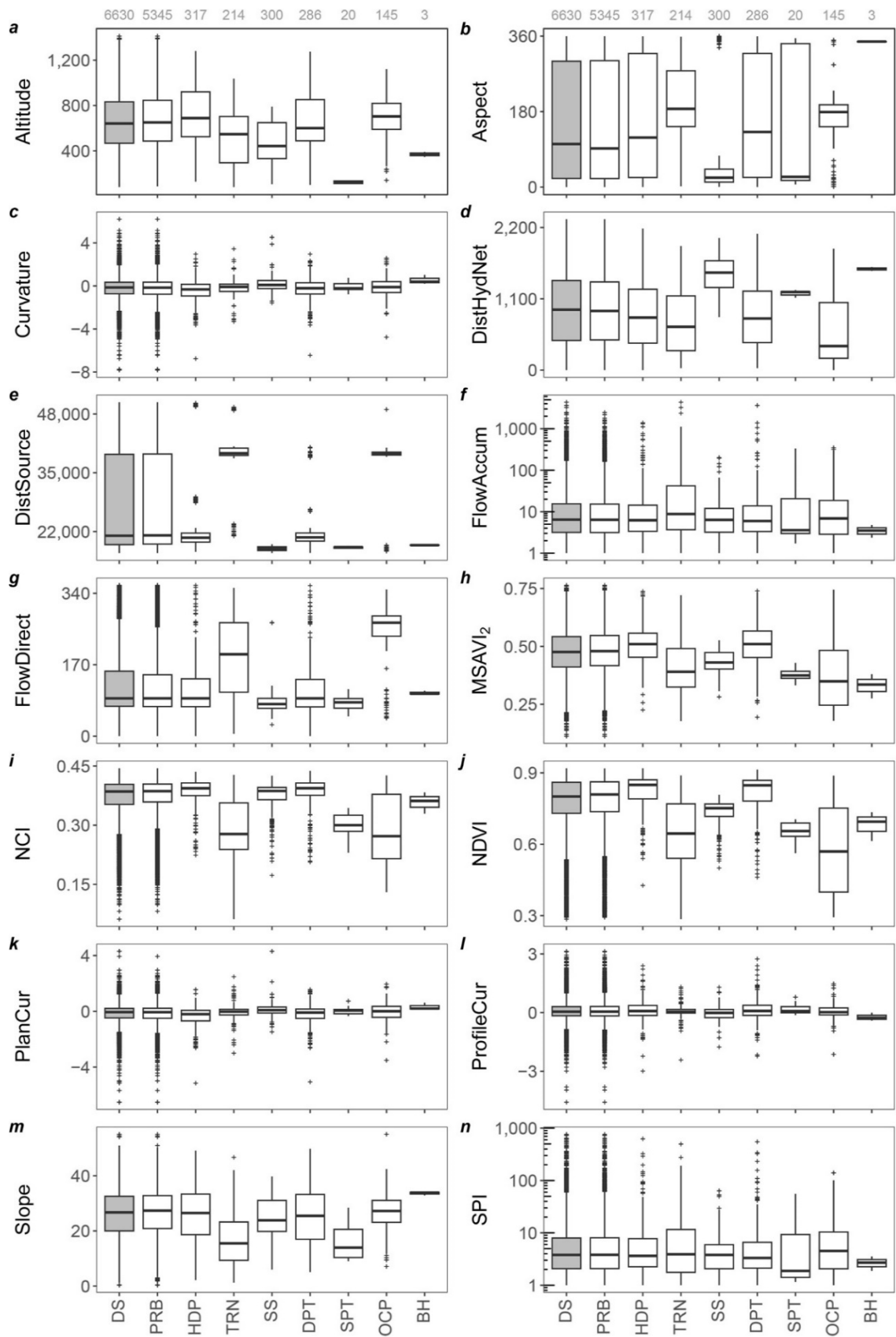
495 **Figure 7: Range of the values for the predictor variables referred to the whole dataset (DS) and the different measurement methods (from PRB to BH). See caption of Fig. 5 for the abbreviations. It is noteworthy that the "partial" measurements (n = 493) are excluded before thickness modelling in this study.**
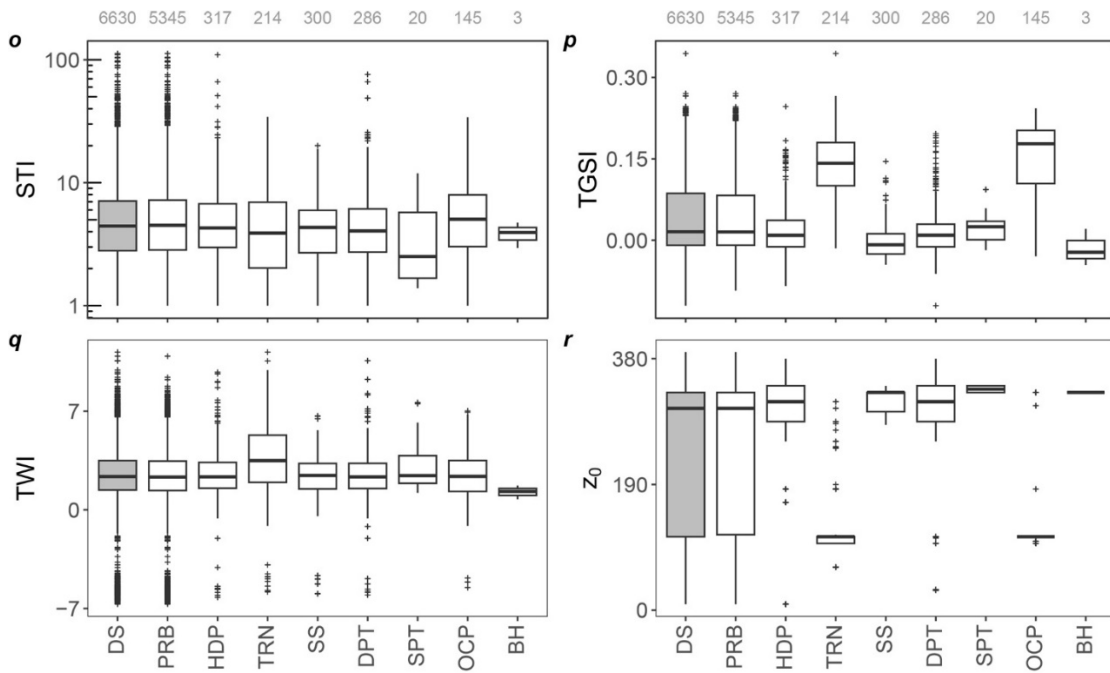
**Figure 7 (continued)**

500
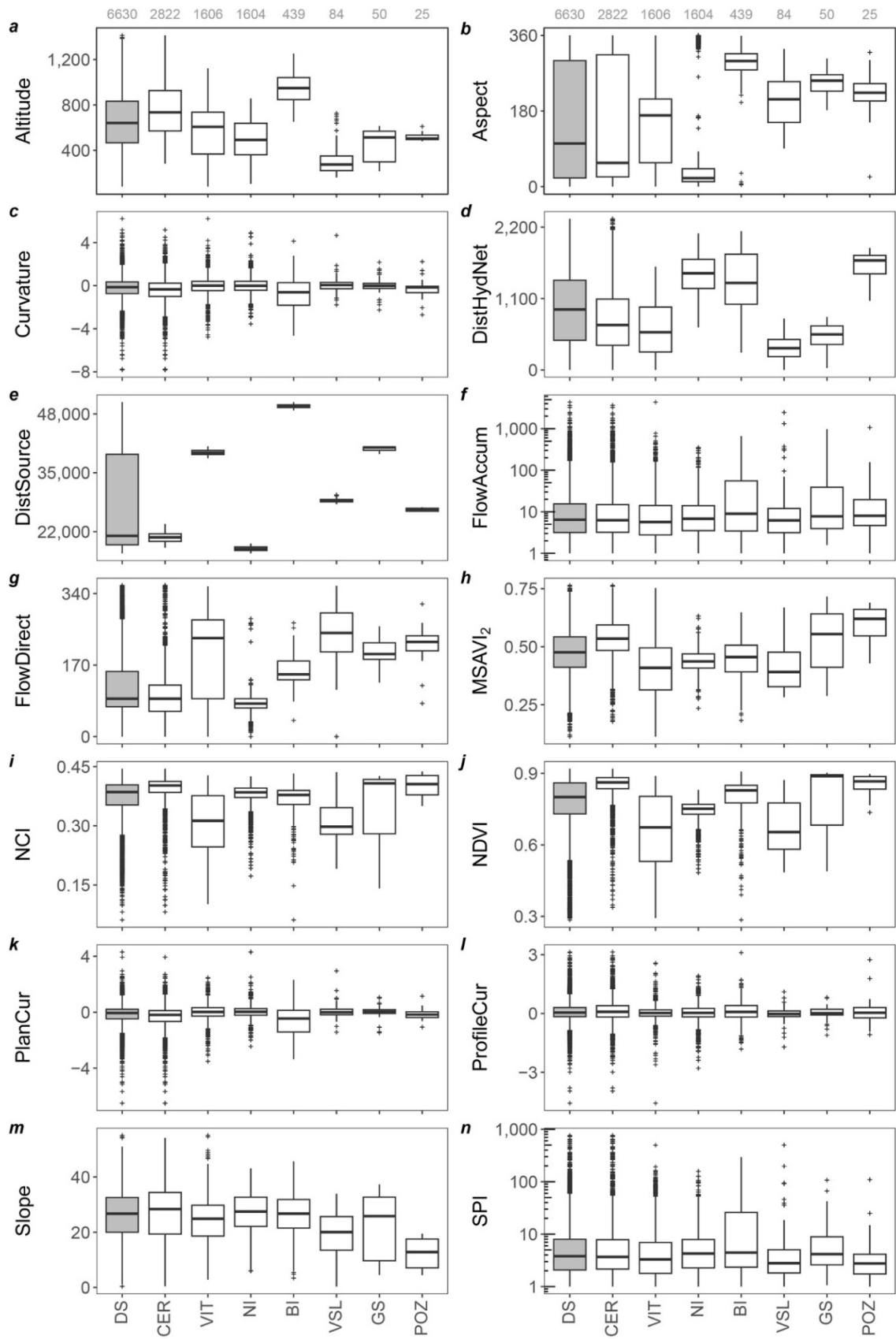
**Figure 8: Range of values for the predictor variables referred to the whole dataset (DS) and the municipalities (from CER to POZ). See caption of Fig. 5 for the abbreviations. It is noteworthy that the "partial" measurements (n = 493) are excluded before thickness modelling in this study.**
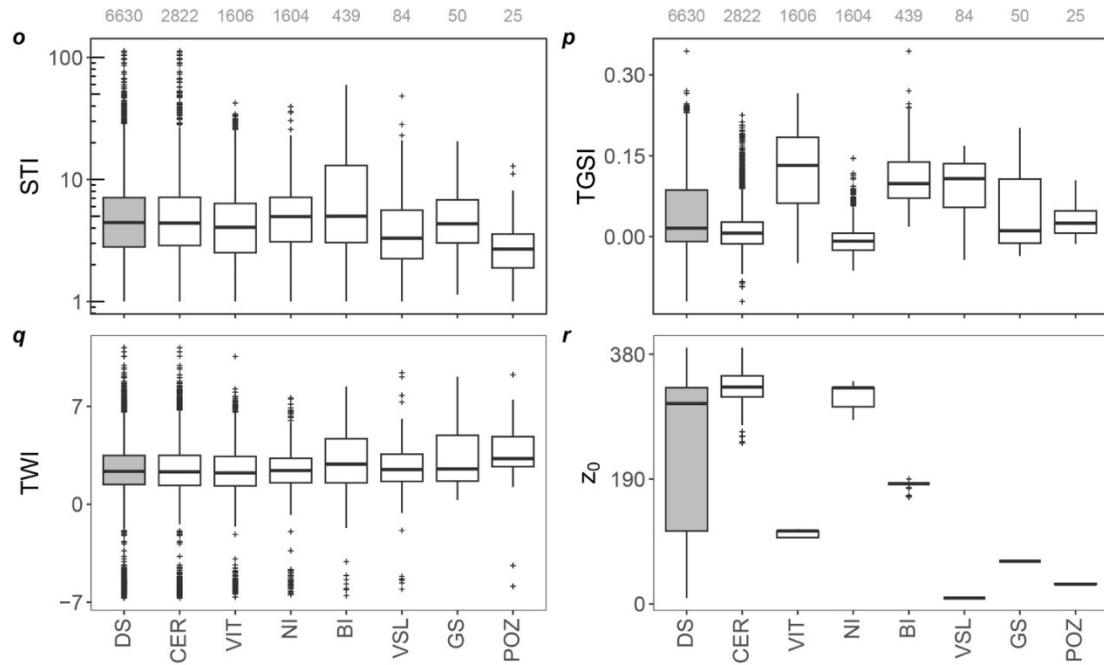
505

**Figure 8 (continued)**

## 5. The estimated thickness of fallout pyroclastic deposits: Results

In this article, we proposed applying RF and STPW approaches that train a model on the training subset and make estimations on the test subset. The dataset of 6137 measurement points was, therefore, randomly divided into training (n = 4294) and test (n = 1843) subsets (Fig. 4) and the same subsets were used in all predictive models to enable evaluating performance of the competing models. On the training data, the thickness is estimated by GPT, SAPT, SEPT, STPW and RF models. The predictions for different models are, then, combined according to the methods in Section 3 (Fig. 3). Finally, the prediction errors are computed on both train and test subset and the predictive accuracy tests are implemented for evaluating differences in the test subset. This section explains the results in detail.

## 5.1. Training stepwise regression and Random Forest

The STPW model is used for selecting the best subset of variables in terms of explicative power for the pyroclastic thickness deposit. Given an initial set of 18 independent variables, only 8 relevant ones are chosen by the STPW model for making predictions (Table 3): distance to the hydrographic network, distance to source, altitude, $z_0$, aspect, plan curvature, $MSAVI_2$ and NCI (for a detailed description of the variables see Table 2). All these variables are very relevant in determining thickness of fallout pyroclastic deposits as they control the erosion-deposition processes. The estimated parameters shown in Table 3 are then used for predicting the thickness values in the test subset.

In order to train Random Forest model representatively, different values are assigned to $m_{try}$, *min.node.size*, *replace* and *sample.fraction* and a list of all possible combinations of the hyperparameters (882 in our case) is generated. Random forest is then trained for all combinations and the optimum value for each hyperparameter ($m_{try}$ = 5; *min.node.size* = 17; *replace* = True; and *sample.fraction* = 0.632) is determined based on the model with the least error. The out-of-bag error is then investigated for different number of trees and *num.trees* = 530 is determined for training a model with the least error (Fig. S1a). Fig. S1b and S1c shows that altitude, $z_0$, NDVI, distance to hydrographic network, NCI and TGSI account for the most important variables in training the model based on both variable importance metrics (i.e. impurity and

permutation). Compared to the STPW model, distance to source is the only variable excluded before RF modelling to avoid unrealistic estimations.

| | Estimated parameter | Standard error | p-value |
|---|---|---|---|
| Intercept | 2.02E+08 | 2.16E+07 | 1.02E-14 |
| DistSource | 9.25E+00 | 3.45E+02 | 9.79E-05 |
| Altitude | -8.28E+04 | 7.66E+03 | 6.53E-21 |
| DistHydNet | 2.19E+04 | 2.79E+03 | 5.63E-09 |
| $z_0$ | 2.87E+05 | 3.43E+04 | 7.81E-11 |
| $MSAVI_2$ | -1.02E+06 | 3.06E+07 | 9.73E-05 |
| PlanCur | 2.65E+06 | 2.55E+06 | 2.97E-05 |
| Aspect | 1.63E+04 | 1.25E+04 | 1.90E-05 |
| NCI | -2.51E+08 | 8.09E+07 | 1.92E-03 |

**Table 3: List of the variables selected by STPW model for making predictions in the training subset. The estimated parameters, standard errors and p-values are also reported.**

### 5.2. Predicted thickness values

Table 4 shows RMSE and MAE for all models, regarding both training and test subsets. The relevant differences in prediction accuracy are evident (e.g. RMSE=184.52 and MAE=157.10 for SAPT vs. RMSE=79.11 and MAE=46.44 for RF). Considering the single models applied to the training subset, both STPW and RF models improve the predictive accuracy measures compared with GPT, SAPT and SEPT. It is worth mentioning that the RF model (RMSE = 79.11 and MAE = 46.44) outperforms other approaches (RMSE > 89 and MAE > 55). This suggests that the predictor variables discussed in section 5.1 play a crucial role in estimating thickness of fallout pyroclastic deposits.

| Category | Model | Train | | Test | |
|---|---|---|---|---|---|
| | | RMSE | MAE | RMSE | MAE |
| Single model | GPT | 95.36 | 56.91 | 94.21 | 56.93 |
| | SAPT | 184.52 | 157.10 | 107.45 | 58.05 |
| | SEPT | 107.20 | 59.75 | 187.95 | 160.31 |
| | STPW | 89.60 | 55.25 | 92.35 | 55.20 |
| | RF | 79.11 | 46.44 | 82.46 | 48.36 |
| Combination approach | SA | 91.64 | 60.82 | 94.22 | 61.86 |
| | MV | **79.05** | 46.05 | 82.51 | 47.97 |
| | OLS | 79.11 | 46.38 | **82.42** | 48.27 |
| | LAD | 80.83 | **44.03** | 83.22 | **45.12** |

**Table 4: Prediction accuracy results. Best model in bold. GPT: Geomorphological Pyroclastic Thickness; SAPT: Slope Angle Pyroclastic Thickness; SEPT: Slope Exponential Pyroclastic Thickness; STPW: Stepwise regression; RF: Random Forest; SA: Simple Average; MV: Minimum Variance; OLS: Ordinary Least Squares; LAD: Least Absolute Deviation.**

In the next step, the thickness predictions for the training subset (obtained from the single models) underwent a combination approach using the weighting schemes in Table 5. Except for the SA method that assigns equal weights to the models, all the weighting schemes assign the largest weight to RF, that is the most accurate one among the single models. The accuracy measures for the combination models are shown in the lower part of Table 4. According to the

results for the training subset (Table 4), the RMSE shows that the predictions of the SA approach are the worst, while the MV approach provides better accuracy than the RF model. The MAE function indicates that the LAD method improves the accuracy about 5% compared to the RF model.

| Weighting scheme | GPT model | SAPT model | SEPT model | STPW model | RF model |
|---|---|---|---|---|---|
| SA | 0.2 | 0.2 | 0.2 | 0.2 | 0.2 |
| MV | 0.04 | -0.03 | -0.07 | 0.07 | 0.99 |
| OLS | 0.00 | 0.00 | 0.01 | 0.00 | 0.99 |
| LAD | -0.1 | 0.03 | -0.08 | -0.09 | 0.96 |

**Table 5: The weights for making predictions in the training subset with combination approaches. The abbreviations are as Table 4.**

Then, both single models and the alternative combination approaches for the test subset are compared in terms of RMSE and MAE (see the last two columns of Table 4). Among the single models, RF provides the most accurate results (RMSE = 82.46 and MAE = 55.20), but combination of the RF predictions with those of the other models enhances the accuracy. In particular, the OLS approach reduces RMSE to 82.42 and the LAD method lowers MAE to 45.12. Regarding less sensitivity of MAE to data outliers, the LAD combination could be considered the most representative model. The LAD combination improved the accuracy by 7.2% compared to the RF model. The improvement is above 26% respect to the GPT model, the best single model proposed in the previous studies.

Finally, pairwise EPA tests are applied to account for the uncertainty in the results and investigate whether the differences in predictive performance are statistically significant in the test subset (Table 6).

| Best single model | Other models | RMSE | SE | MAE | SE |
|---|---|---|---|---|---|
| RF vs. | GPT | -2650.0*** | 705.2 | -8.564*** | 1.113 |
| | SAPT | -4745.0*** | 821.5 | -9.689*** | 1.4320 |
| | SEPT | -28523.4*** | 753.6 | -111.94*** | 2.2730 |
| | STPW | -1729.0*** | 533.6 | -6.8339*** | 0.9109 |
| | SA | -2076.229*** | 432.758 | -13.493*** | 0.953 |
| | MV | -7.006 | 10.328 | 0.390*** | 0.066 |
| | OLS | 5.971 | 6.188 | 0.091*** | 0.013 |
| | LAD | -125.269 | 126.711 | 3.245*** | 0.397 |

**Table 6. Equal predictive accuracy tests, applied to the test subset (n = 1843), for comparing the best single model (RF) with the other ones. Under the null hypothesis, the two models provide equal predictive accuracy. SE refers to the heteroskedasticity robust standard error. The abbreviations are as Table 4. *** indicates p-value<0.01.**

The upper part of Table 6 compares RF as the best single model with the other single models and reveals that the differences are statistically significant. In other words, the observed differences in predictive performance of the models are not explained by randomness of the data, and RF model provides the most accurate thickness estimation. The negative RMSE and MAE values indicate that the RF model has a lower average prediction error than the other single models. On the other hand, the lower part of Table 6 shows the pairwise comparison of the RF model with all the combination approaches. A positive RMSE or MAE value suggests that the predictions of the combination approach are more accurate. In terms of squared error loss, the OLS combination approach provides the most accurate predictions than the RF model,

but it is noteworthy that RMSE and OLS are both sensitive to data outliers as explained in Section 3.3. Regarding the MAE, statistically significant improvement is observed when combination approaches are applied (except for the SA method; $p < 0.01$). The greatest statistically significant constant value of the LAD method demonstrates that this combination technique is suitable for predicting thickness of fallout pyroclastic deposits in unmeasured locations. The results are in accordance with those in Table 4.

## 6. Discussion

In this section, cumulative probability of the estimated thickness (for both train and test subsets) by various methods are compared in Fig. 9a,b. Regarding the single models (Fig. 9a), significant underestimation of the SEPT model and noticeable overestimation of the SAPT model are evident. These models have the highest RMSE and MAE values among the single models (Table 4). Distribution of the values obtained by the GPT, RF and STPW models share more similarity with that of field-based measurements. Although the STPW model performs better than RF in predicting the smaller values, the RF model outperforms the single models which agrees with Table 4. Taking Fig. 9b into account, all combination techniques work more effectively than the LAD approach in the upper 25% of thickness values. The overall estimations of LAD approach are, however, more consistent with the field-based measurements, being confirmed by the accuracy measures in Table 4.

The results of RF model and LAD approach are also visualized in Fig. 9c for the sake of comparison, representing that the values estimated by former are greater than those of the latter. The LAD approach outperforms the RF model in a wide range of the field-based thickness values, and it is, therefore, the best model for predicting thickness of fallout pyroclastic deposits in the study area. Fig. 9d demonstrates that the LAD estimations are less biased.

The estimated thickness values of fallout pyroclastic deposits by the RF model and the LAD combination approach in Vitulano, Cervinara and Nocera Inferiore are visualized in Figs. 10-12 to investigate the differences between the spatial patterns. Although the spatial distribution remained generally unchanged, legends of the maps reveal that the estimated thickness values by the LAD combination approach decreased as shown before (Fig. 9c). For instance, in Vitulano (Fig. 10), the estimations range from 10-196 cm in the RF model which is reduced to 1-177 cm in the LAD combination approach. This is also evident in most estimations of the bottom-right box in which the values reduce from 66-94 cm to about 32-66 cm or in the top-left corner of the map: A (47-196 cm) > C (32-66 cm) > B (32-47cm) in the RF model vs. A (47-94 cm) > C (32-47 cm) > B (1-32 cm) in the LAD combination approach. The same decline could be observed in Cervinara and Nocera Inferiore as well. To facilitate a quick comparison, two boxes are drawn on Figs. 11 and 12 that highlight the sectors with a clear change. A few estimations exceed 113 cm in the lower panel of Fig. 11, being contrary to the upper panel generated by the RF model in Cervinara.

610
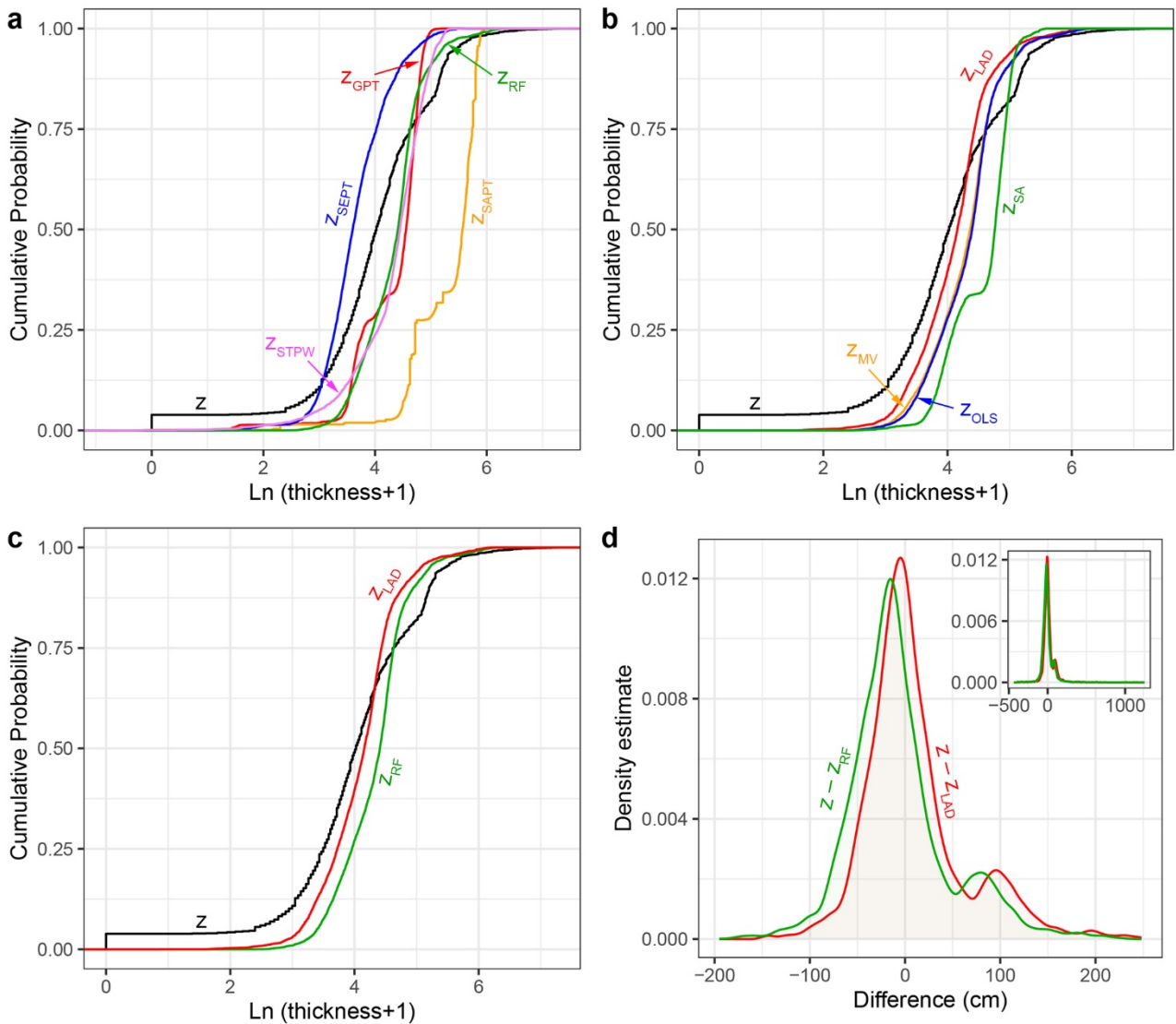
**Figure 9: Cumulative probability of the field-based thickness measurements (z) against the estimations by single models and combination approaches (a and b, respectively). In panel c, only z, the estimations by the best single model and the best combination approach are visualized. However, panel d represents the difference between z and the estimated thickness by the best single model and the best combination technique. In this figure, z represents thickness, but the subscript refers to the method of estimation. The estimations (n = 6137) for both training and test subsets are visualized. GPT: Geomorphological Pyroclastic Thickness; SAPT: Slope Angle Pyroclastic Thickness; SEPT: Slope Exponential Pyroclastic Thickness; STPW: Stepwise regression; RF: Random Forest; SA: Simple Average; MV: Minimum Variance; OLS: Ordinary Least Squares; LAD: Least Absolute Deviation.**
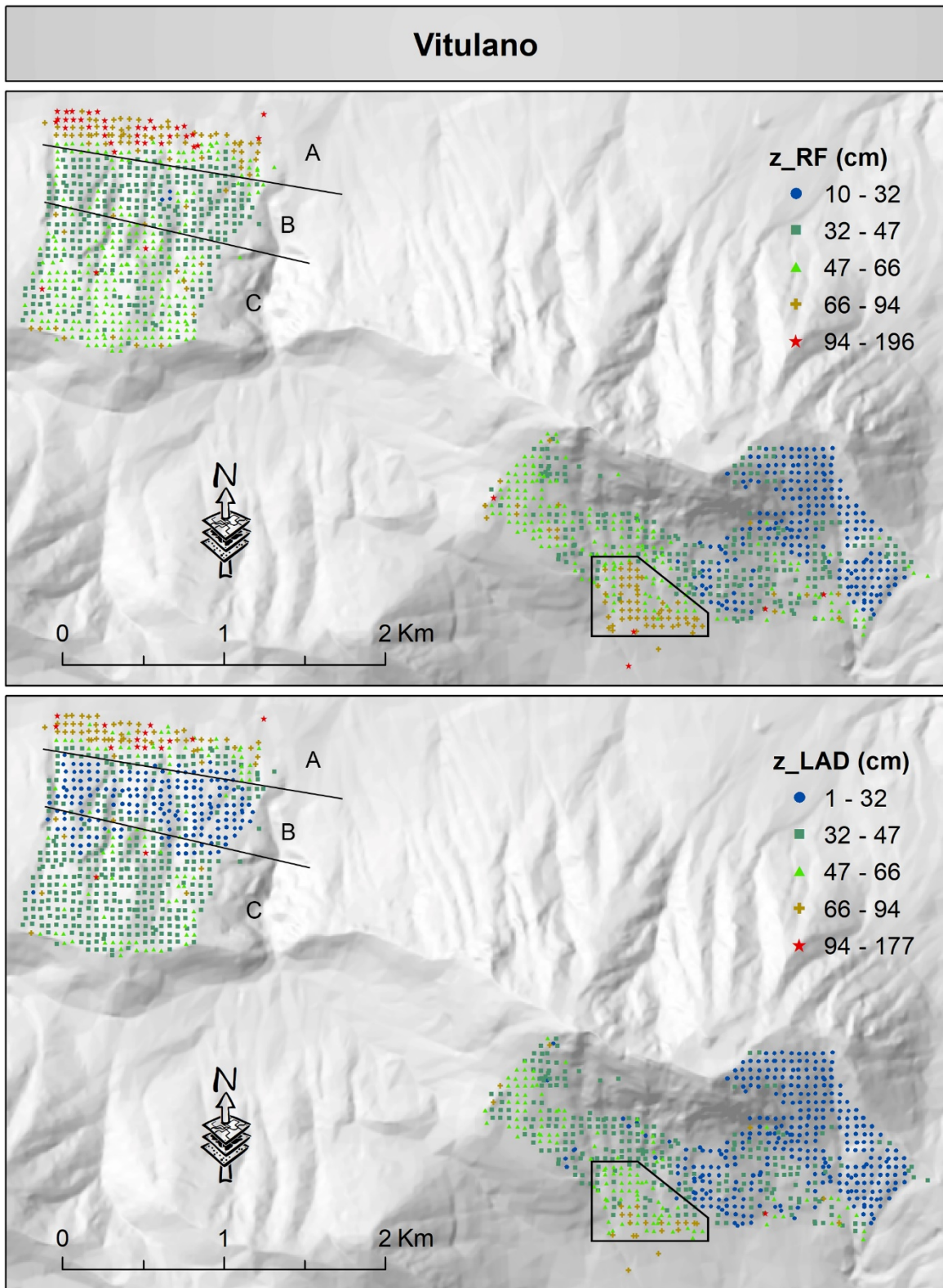
**Figure 10: Spatial visualization of the predicted thickness of fallout pyroclastic deposits by Random Forest as the best single model (the upper panel) and by LAD as the best combination approach (the lower panel) for Vitulano municipality. It is worth mentioning that the Random Forest predictions are classified by the natural breaks method and the thresholds are implemented for generating the map of LAD predictions. Please see the text for more information about A, B and C labels together with the black box. Although symbols of different shapes and colours are used for the classes, the spatially dense measurement points do not allow applying a larger symbol size. In the electronic version of this article, please zoom in on the figure to distinguish between different symbols based on the shape (if required).**
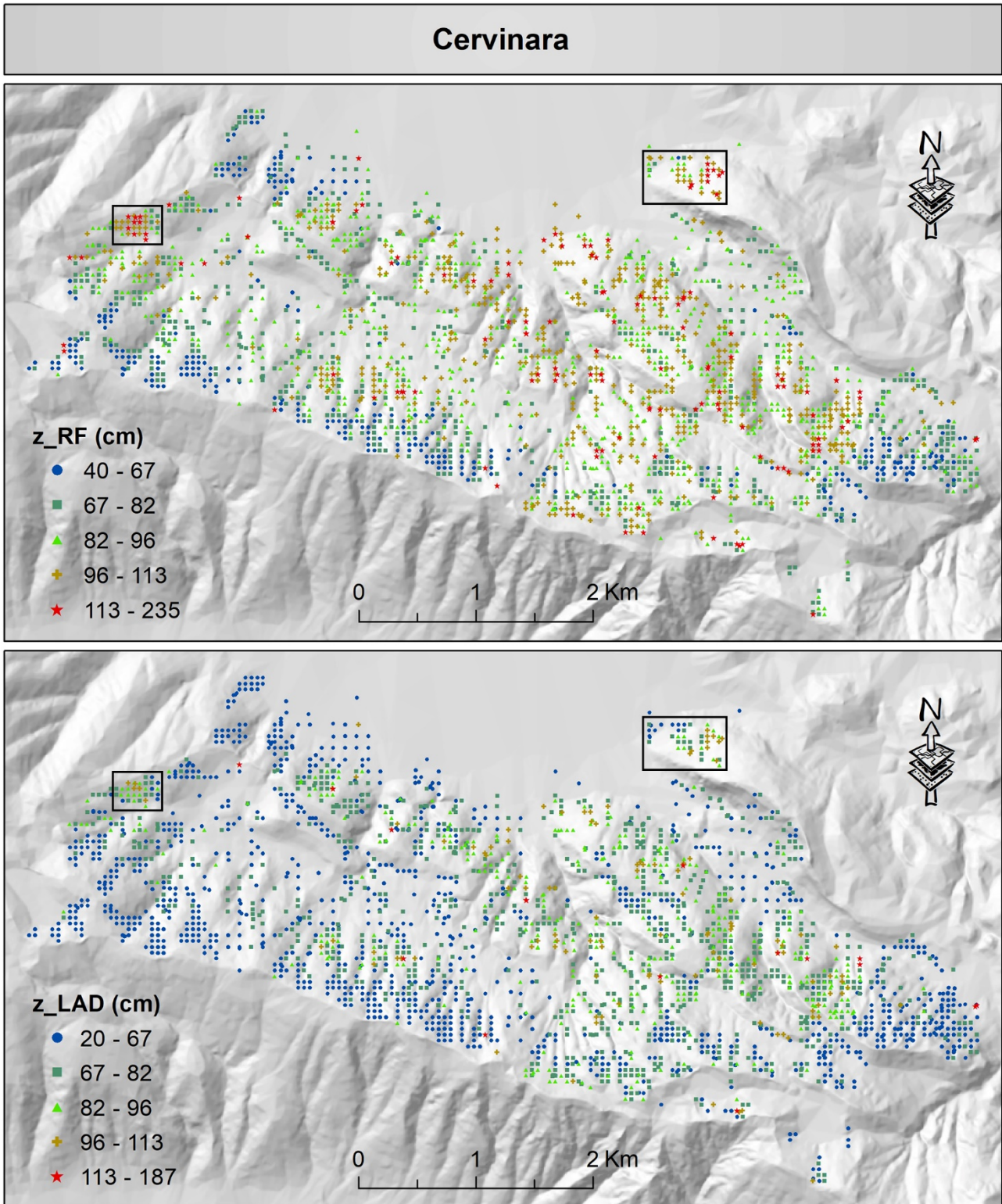
Figure 11: Spatial visualization of the predicted thickness of fallout pyroclastic deposits by Random Forest as the best single model (the upper panel) and by LAD as the best combination approach (the lower panel) for Cervinara municipality. It is worth mentioning that the Random Rorest predictions are classified by the natural breaks method and the thresholds are implemented for generating the map of LAD predictions. Please see the text for more information about the black boxes. Although symbols of different shapes and colours are used for the classes, the spatially dense measurement points do not allow applying a larger symbol size. In the electronic version of this article, please zoom in on the figure to distinguish between different symbols based on the shape (if required).
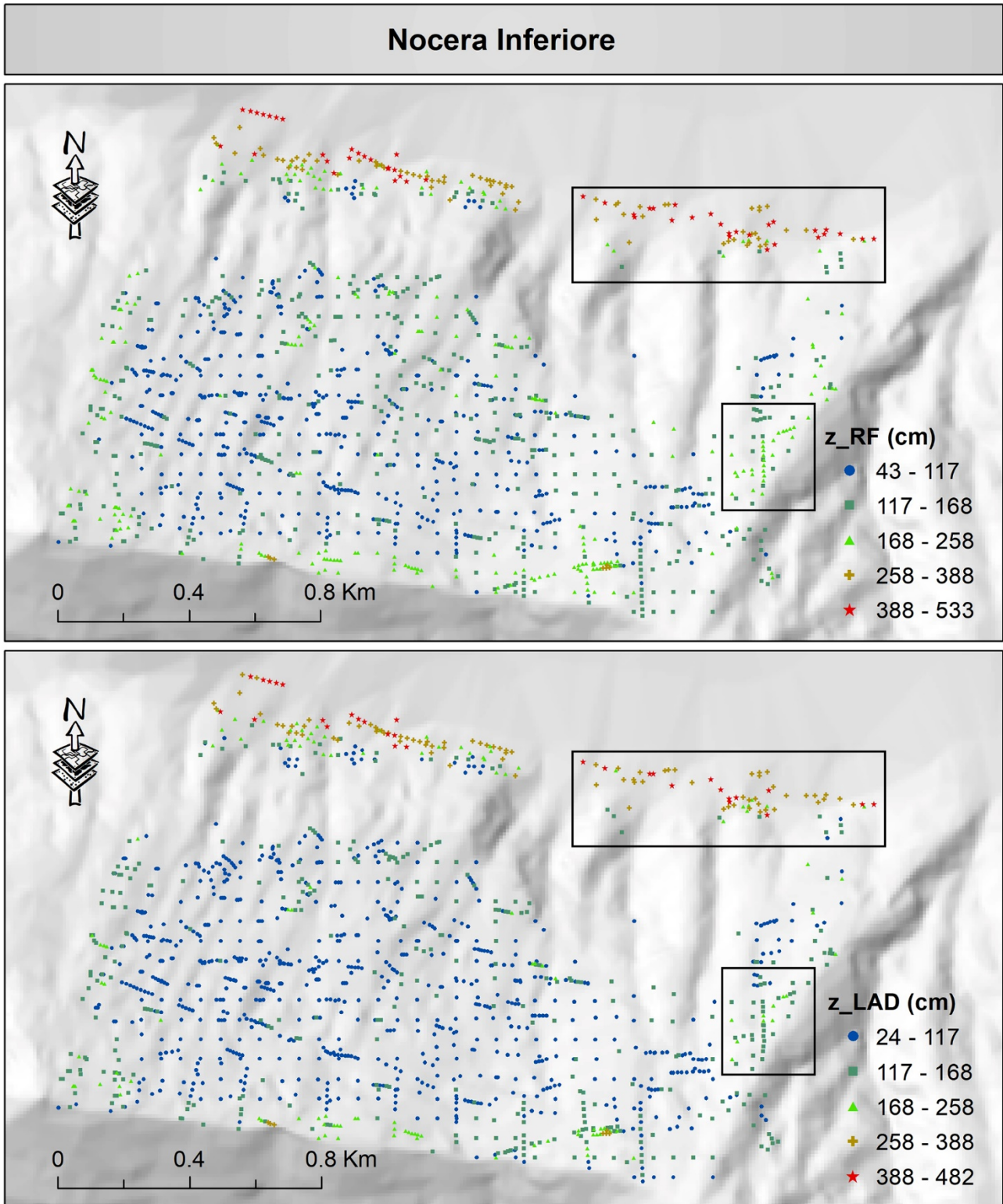
**Figure 12: Spatial visualization of the predicted thickness of fallout pyroclastic deposits by Random Forest as the best single model (the upper panel) and by LAD as the best combination approach (the lower panel) for Nocera Inferiore municipality. It is worth mentioning that the RF predictions are classified by the natural breaks method and the thresholds are implemented for generating the map of LAD predictions. Please see the text for more information about the black boxes. Although symbols of different shapes and colours are used for the classes, the spatially dense measurement points do not allow applying a larger symbol size. In the electronic version of this article, please zoom in on the figure to distinguish between different symbols based on the shape (if required).**

**7. Data availability**

The field-based thickness measurements of fallout pyroclastic deposits are accessible on Zenodo (Matano et al., 2023; https://doi.org/10.5281/zenodo.8399487).

650

**8. Conclusion and future research direction**

A given volcano might have several eruptive events. In an explosive volcanic eruption, the height of ash plume and wind characteristics mainly determine the ash-dispersal pattern. However, the expected spatial thickness may be continuously altered by the soil forming and denudation processes. It is, therefore, a daunting task to estimate thickness of fallout
655 pyroclastic deposits that we observe today. The GPT, SAPT and SEPT models were proposed in the previous studies to address this issue, but this article tries to apply other models for the first time to estimate thickness more accurately around the Somma-Vesuvius, Phlegrean Fields and Roccamonfina volcanoes in Campania region, south Italy.

First, we prepared a database of 6137 field-based thickness measurements with 18 predictor variables. Second, the STPW model and the RF machine learning technique were implemented for thickness modelling and the results were compared
660 with those of GPT, SAPT and SEPT models. The RF estimations (RMSE = 79.11 and MAE = 46.44 for the training subset, and RMSE = 82.46 and MAE = 48.36 for the test subset) evidently outperformed the other models (RMSE > 89.60 and MAE > 55.25 for the training subset, and RMSE = 92.35 and MAE > 55.20 for the test subset). Third, the SA, LAD, MV and OLS approaches were considered to combine the predictions of the above-mentioned five single models and to obtain more accurate thickness estimations. It was indicated that the LAD approach returns the best results in terms of
665 MAE. Thus, the estimations with the RF and LAD methods (as a single model and a combination approach, respectively) were less biased in Campania region. The thickness values obtained from the RF and LAD in Vitulano, Cervinara and Nocera Inferiore were applied for spatial analysis and it was demonstrated that the estimated values of the LAD approach are smaller than those of RF, but the spatial patterns do not change significantly. The results showed that following the methodology in this article and generating a map by the estimations of the LAD combination approach provides the most
670 representative estimations in the study area.

In the future, we consider a set of more representative predictor variables (if any) and collect a larger field-based thickness measurement dataset for estimating thickness in the unmeasured locations (i.e. out-of-sample predictions from statistical point of view) more accurately. It would help generate a regional map of thickness of fallout pyroclastic deposits in Campania region which plays a key role in hydrogeological and volcanological studies and in managing geohazards in
675 the areas covered with loose pyroclastic materials. Furthermore, we aim to define the best statistical combinations at local levels by means of clusterwise techniques.

**Author contribution**

All authors wrote the original draft and revised the manuscript. FM, PE and VA: geology, geomorphology and volcanological history; RM, GS and PE: statistical analyses; FM: Field measurements and supervision of the research
680 activity.

**Competing interests**

The authors declare that they have no conflict of interest.

**Acknowledgements**

The authors acknowledge Prof. Paola Petrosino for suggestions about volcanic history of the study area. Thanks are
685    extended to Dr. Massimo Cesarano and Dr. Annarita Casabduri for the constructive comments.

**References**

Albert, P. G., Giaccio, B., Isaia, R., Costa, A., Niespolo, E. M., Nomade, S., ... & Smith, V. C. (2019). Evidence for a large-magnitude eruption from Campi Flegrei caldera (Italy) at 29 ka. Geology, 47(7), 595-599. https://doi.org/10.1130/G45805.1

690    Amato, V., Aucelli, P. P. C., Cesarano, M., Filocamo, F., Leone, N., Petrosino, P., ... & Jicha, B. R. (2018). Geomorphic response to late Quaternary tectonics in the axial portion of the Southern Apennines (Italy): A case study from the Calore River valley. Earth Surface Processes and Landforms, 43(11), 2463-2480. https://doi.org/10.1002/esp.4390

Andronico, D., Calderoni, G., Cioni, R., Sbrana, A., Sulpizio, R., & Santacroce, R. (1995). Geological map of Somma-Vesuvius volcano. Periodico di Mineralogia, 64 (1-2), 77-78.

695    Andronico, D., & Cioni, R. (2002). Contrasting styles of Mount Vesuvius activity in the period between the Avellino and Pompeii Plinian eruptions, and some implications for assessment of future hazards. Bulletin of Volcanology, 64, 372-391. https://doi.org/10.1007/s00445-002-0215-4

Arrighi, S., Principe, C., & Rosi, M. (2001). Violent strombolian and subplinian eruptions at Vesuvius during post-1631 activity. Bulletin of Volcanology, 63, 126-150. https://doi.org/10.1007/s004450100130

700    Aulinas, M., Civetta, L., Di Vito, M. A., Orsi, G., Gimeno, D., & Férnandez-Turiel, J. L. (2008). The "Pomici di mercato" Plinian eruption of Somma-Vesuvius: magma chamber processes and eruption dynamics. Bulletin of Volcanology, 70, 825-840. https://doi.org/10.1007/s00445-007-0172-z

Barberi, F., Innocenti, F., Lirer, L., Munno, R., Pescatore, T., & Santacroce, R. (1978). The Campanian Ignimbrite: a major prehistoric eruption in the Neapolitan area (Italy). Bulletin Volcanologique, 41, 10-31.
705    https://doi.org/10.1007/BF02597680

Bates, J. M., & Granger, C. W. (1969). The combination of predictions. Journal of the Operational Research Society, 20(4), 451-468.

Bertagnini, A., Cioni, R., Guidoboni, E., Rosi, M., Neri, A., & Boschi, E. (2006). Eruption early warning at Vesuvius: The AD 1631 lesson. Geophysical research letters, 33(18). https://doi.org/10.1029/2006GL027297

710    Beven, K. J., & Kirkby, M. J. (1979). A physically based, variable contributing area model of basin hydrology/Un modèle à base physique de zone d'appel variable de l'hydrologie du bassin versant. Hydrological Sciences Journal, 24(1), 43-69. https://doi.org/10.1080/02626667909491834

Bonardi, G., Ciarcia, S., Di Nocera, S., Matano, F., Sgrosso, I., & Torre, M. (2009). Carta delle principali unità cinematiche dell'Appennino meridionale. Nota illustrativa. Bollettino della Società Geologica Italiana, 128(1), 47-60.

715    Boncio, P., Auciello, E., Amato, V., Aucelli, P. P., Petrosino, P., Tangari, A. C., & Jicha, B. R. (2022). Late Quaternary faulting in the southern Matese (Italy): implications for earthquake potential and slip rate variability in the southern Apennines. Solid Earth, 13, 553–582. https://doi.org/10.5194/se-13-553-2022.

Bourne, A. J., Lowe, J. J., Trincardi, F., Asioli, A., Blockley, S. P. E., Wulf, S., ... & Vigliotti, L. (2010). Distal tephra record for the last ca 105,000 years from core PRAD 1-2 in the central Adriatic Sea: implications for marine
720    tephrostratigraphy. Quaternary Science Reviews, 29(23-24), 3079-3094. https://doi.org/10.1016/j.quascirev.2010.07.021

Brown, R. J., Bonadonna, C., & Durant, A. J. (2012). A review of volcanic ash aggregation. Physics and Chemistry of the Earth, Parts a/b/c, 45, 65-78. https://doi.org/10.1016/j.pce.2011.11.001

Burrough, P. A., & McDonell, R. A., (1998). Principles of Geographical Information Systems. Oxford University Press, New York.

Cannatelli, C., Spera, F. J., Bodnar, R. J., Lima, A., & De Vivo, B. (2020). Ground movement (bradyseism) in the Campi Flegrei volcanic area: a review. Editor(s): De Vivo, B., Belkin, H. E., Rolandi, G., Vesuvius, Campi Flegrei, and Campanian Volcanism, Elsevier, 2020, 407-433. https://doi.org/10.1016/B978-0-12-816454-9.00015-8

Cappelletti, P., Cerri, G., Colella, A., de'Gennaro, M., Langella, A., Perrotta, A., & Scarpati, C. (2003). Post-eruptive processes in the Campanian Ignimbrite. Mineralogy and Petrology, 79, 79-97. https://doi.org/10.1007/s00710-003-0003-7

Caron, B., Siani, G., Sulpizio, R., Zanchetta, G., Paterne, M., Santacroce, R., ... & Zanella, E. (2012). Late Pleistocene to Holocene tephrostratigraphic record from the northern Ionian Sea. Marine Geology, 311, 41-51. https://doi.org/10.1016/j.margeo.2012.04.001

Chan, F., & Pauwels, L. L. (2018). Some theoretical results on prediction combinations. International Journal of Predictioning, 34(1), 64-74.

Chiodini, G., Frondini, F., Cardellini, C., Granieri, D., Marini, L., & Ventura, G. (2001). $CO_2$ degassing and energy release at Solfatara volcano, Campi Flegrei, Italy. Journal of Geophysical Research: Solid Earth, 106(B8), 16213-16221, https://doi.org/10.1029/2001JB000246

Cioni, R., Sulpizio, R., & Garruccio, N. (2003). Variability of the eruption dynamics during a subplinian event: The Greenish Pumice eruption of Somma-Vesuvius (Italy). Journal of Volcanology and Geothermal Research, 124, 89–114. https://doi.org/10.1016/S0377-0273(03)00070-2

Cioni, R., Pistolesi, M., & Rosi, M. (2015). Plinian and Subplinian Eruptions. In: Encyclopedia of Volcanoes, 2nd Ed. Elsevier Science Publishing. https://doi.org/10.1016/B978-0-12-385938-9.00029-8

Civetta, L., Orsi, G., Pappalardo, L., Fisher, R. V., Heiken, G., & Ort, M. (1997). Geochemical zoning, mingling, eruptive dynamics and depositional processes—the Campanian Ignimbrite, Campi Flegrei caldera, Italy. Journal of Volcanology and Geothermal Research, 75(3-4), 183-219. https://doi.org/10.1016/S0377-0273(96)00027-3

Costa, A., Dell'Erba, F., Di Vito, M. A., Isaia, R., Macedonio, G., Orsi, G., & Pfeiffer, T. (2009). Tephra fallout hazard assessment at the Campi Flegrei caldera (Italy). Bulletin of Volcanology, 71, 259-273. https://doi.org/10.1007/s00445-008-0220-3

Costa, A., Folch, A., Macedonio, G., Giaccio, B., Isaia, R., & Smith, V. C. (2012). Quantifying volcanic ash dispersal and impact of the Campanian Ignimbrite super-eruption. Geophysical Research Letters, 39(10). https://doi.org/10.1029/2012GL051605

Costa, A., Di Vito, M. A., Ricciardi, G. P., Smith, V. C., & Talamo, P. (2022). The long and intertwined record of humans and the Campi Flegrei volcano (Italy). Bulletin of Volcanology, 84, 1-27. https://doi.org/10.1007/s00445-021-01503-x

Cui, S., Yin, Y., Wang, D., Li, Z., & Wang, Y. (2021). A stacking-based ensemble learning method for earthquake casualty prediction. Applied Soft Computing, 101, 107038. https://doi.org/10.1016/j.asoc.2020.107038

Cuomo, S., Masi, E. B., Tofani, V., Moscariello, M., Rossi, G., & Matano, F. (2021). Multiseasonal probabilistic slope stability analysis of a large area of unsaturated pyroclastic soils. Landslides, 18, 1259-1274. https://doi.org/10.1007/s10346-020-01561-w

760      de Lorenzo, S., Gasparini, P., Mongelli, F., & Zollo, A. (2001). Thermal state of the Campi Flegrei caldera inferred from seismic attenuation tomography. Journal of geodynamics, 32(4-5), 467-486. https://doi.org/10.1016/S0264-3707(01)00044-8

De Vita, P., & Nappi, M. (2013). Regional distribution of ash-fall pyroclastic soils for landslide susceptibility assessment. In Margottini, C., Canuti, P., Sassa, K. (Eds.). Landslide Science and Practice. Springer, Berlin, Heidelberg; pp. 103-109.

765      https://doi.org/10.1007/978-3-642-31310-3_15

De Vita, P., Agrello, D., & Ambrosino, F. (2006a). Landslide susceptibility assessment in ash-fall pyroclastic deposits surrounding Mount Somma-Vesuvius: Application of geophysical surveys for soil thickness mapping. Journal of Applied Geophysics, 59(2), 126-139. https://doi.org/10.1016/j.jappgeo.2005.09.001

De Vita, S., Sansivero, F., Orsi, G., & Marotta, E. (2006b). Cyclical slope instability and volcanism related to volcano-

770      tectonism in resurgent calderas: the Ischia island (Italy) case study. Engineering Geology, 86(2-3), 148-165. https://doi.org/10.1016/j.enggeo.2006.02.013

De Vita, S., Orsi, G., Civetta, L., Carandente, A., D'Antonio, M., Deino, A., ... & Southon, J. (1999). The Agnano–Monte Spina eruption (4100 years BP) in the restless Campi Flegrei caldera (Italy). Journal of Volcanology and Geothermal Research, 91(2-4), 269-301. https://doi.org/10.1016/S0377-0273(99)00039-6

775      De Vivo, B., Rolandi, G., Gans, P. B., Calvert, A., Bohrson, W. A., Spera, F. J., & Belkin, H. E. (2001). New constraints on the pyroclastic eruptive history of the Campanian volcanic Plain (Italy). Mineralogy and Petrology, 73, 47-65. https://doi.org/10.1007/s007100170010

Deino, A. L., Orsi, G., De Vita, S., & Piochi, M. (2004). The age of the Neapolitan Yellow Tuff caldera-forming eruption (Campi Flegrei caldera–Italy) assessed by 40Ar/39Ar dating method. Journal of Volcanology and Geothermal Research,

780      133(1-4), 157-170. https://doi.org/10.1016/S0377-0273(03)00396-2

Dellino, P., Dioguardi, F., Isaia, R., Sulpizio, R., & Mele, D. (2021). The impact of pyroclastic density currents duration on humans: the case of the AD 79 eruption of Vesuvius. Scientific Reports, 11(1), 4959. https://doi.org/10.1038/s41598-021-84456-7

Del Soldato, M., Pazzi, V., Segoni, S., De Vita, P., Tofani, V., & Moretti, S. (2018). Spatial modeling of pyroclastic cover

785      deposit thickness (depth to bedrock) in peri-volcanic areas of Campania (southern Italy). Earth Surface Processes and Landforms, 43(9), 1757-1767. https://doi.org/10.1002/esp.4350

Del Soldato, M., Segoni, S., De Vita, P., Pazzi, V., Tofani, V., & Moretti, S. (2016). Thickness model of pyroclastic soils along mountain slopes of Campania (southern Italy). In Aversa, S., Cascini, L., Picarelli, L., & Scavia C. (Eds.). Landslides and engineered slopes. Experience, theory and practice. Proceedings of the 12th International Symposium on

790      Landslides, Napoli, Italy, 12–19 June. CRC Press: Boca Raton, FL; pp. 797-804.

De Vivo, B., Rolandi, G., Gans, P., Calvert A., Bohrson W. A., Spera F. J. & Belkin H. E. (2001). New constraints on the pyroclastic eruptive history of the Campanian volcanic Plain (Italy). Mineralogy and Petrology 73, 47–65. https://doi.org/10.1007/s007100170010

Di Nocera, S., Matano, F., Pescatore, T., Pinto, F., Quarantiello, R., Senatore, M., & Torre, M. (2006). Schema geologico

795      del transetto Monti Picentini orientali–Monti della Daunia meridionali: unità stratigrafiche ed evoluzione tettonica del settore esterno dell'Appennino meridionale. Bollettino della Società Geologica Italiana, 125, 39-58.

Di Renzo, V., Arienzo, I., Civetta, L., D'Antonio, M., Tonarini, S., Di Vito, M. A., & Orsi, G. (2011). The magmatic feeding system of the Campi Flegrei caldera: architecture and temporal evolution. Chemical Geology, 281(3-4), 227-241. https://doi.org/10.1016/j.chemgeo.2010.12.010

800     Di Vito, M. A., Talamo, P., de Vita, S., Rucco, I., Zanchetta, G., & Cesarano, M. (2019). Dynamics and effects of the Vesuvius Pomici di Avellino Plinian eruption and related phenomena on the Bronze Age landscape of Campania region (Southern Italy). Quaternary International, 499, 231-244. https://doi.org/10.1016/j.quaint.2018.03.021

Di Vito, M., Lirer, L., Mastrolorenzo, G., & Rolandi, G. (1987). The 1538 Monte Nuovo eruption (Campi Flegrei, Italy). Bulletin of Volcanology, 49, 608-615. https://doi.org/10.1007/BF01079966

805     Di Vito, M. A., Isaia, R., Orsi, G., Southon, J. D., De Vita, S., D'Antonio, M., ... & Piochi, M. (1999). Volcanism and deformation since 12,000 years at the Campi Flegrei caldera (Italy). Journal of Volcanology and Geothermal Research, 91(2-4), 221-246. https://doi.org/10.1016/S0377-0273(99)00037-2

Di Vito, M. A., Acocella, V., Aiello, G., Barra, D., Battaglia, M., Carandente, A., ... & Terrasi, F. (2016). Magma transfer at Campi Flegrei caldera (Italy) before the 1538 AD eruption. Scientific Reports, 6(1), 32245.

810     https://doi.org/10.1038/srep32245

Di Vito, M. A., Sulpizio, R., Zanchetta, G., & D'Orazio, M. (2008). The late Pleistocene pyroclastic deposits of the Campanian Plain: new insights into the explosive activity of Neapolitan volcanoes. Journal of Volcanology and Geothermal Research, 177(1), 19-48. https://doi.org/10.1016/j.jvolgeores.2007.11.019

Di Vito, M. A., Aurino, P., Boenzi, G., Laforgia, E., & Rucco, I. (2021). Human communities living in the central

815     Campania Plain during eruptions of Vesuvius and Campi Flegrei. Annals of Geophysics, 64(5), VO546. https://doi.org/10.4401/ag-8708

Doglioni, C. (1991). A proposal for the kinematic modelling of W-dipping subductions-possible applications to the Tyrrhenian-Apennines system. Terra nova, 3(4), 423-434. https://doi.org/10.1144/SP288.3

Ducci, D., & Tranfaglia, G. (2008). Effects of climate change on groundwater resources in Campania (southern Italy).

820     Geological Society, London, Special Publications, 288(1), 25-38. https://doi.org/10.1144/SP288.3

Doronzo, D. M., Di Vito, M. A., Arienzo, I., Bini, M., Calusi, B., Cerminara, M., ... & Zanchetta, G. (2022). The 79 CE eruption of Vesuvius: A lesson from the past and the need of a multidisciplinary approach for developments in volcanology. Earth-Science Reviews, 231, 104072. https://doi.org/10.1016/j.earscirev.2022.104072

Engwell, S. L., Sparks, R. S. J., & Carey, S. (2014). Physical characteristics of tephra layers in the deep sea realm: the

825     Campanian Eruption. Geological Society, London, Special Publications, 398(1), 47-64. https://doi.org/10.1144/SP398.7

Elliott, G., & Timmermann, A. (2004). Optimal forecast combinations under general loss functions and forecast error distributions. Journal of Econometrics, 122(1), 47-79. https://doi.org/10.1016/j.jeconom.2003.10.019

Eychenne, J., & Engwell, S. L. (2023). The grainsize of volcanic fall deposits: Spatial trends and physical controls. GSA Bulletin, 135(7-8), 1844-1858. https://doi.org/10.1130/B36275.1

830     Ferranti, L., & Oldow, J. S. (2005). Latest Miocene to Quaternary horizontal and vertical displacement rates during simultaneous contraction and extension in the Southern Apennines orogen, Italy. Terra Nova, 17(3), 209-214. https://doi.org/10.1111/j.1365-3121.2005.00593.x

Fisher, R. V., Orsi, G., Ort, M., & Heiken, G. (1993). Mobility of a large-volume pyroclastic flow—emplacement of the Campanian ignimbrite, Italy. Journal of Volcanology and Geothermal Research, 56(3), 205-220.

835     https://doi.org/10.1016/0377-0273(93)90017-L

Frick, H., Chow, F., Kuhn, M., Mahoney, M., Silge, J., & Wickham, H. (2022). _rsample: General Resampling Infrastructure_. R package version 1.1.1, https://CRAN.R-project.org/package=rsample

Ganaie, M. A., Hu, M., Malik, A. K., Tanveer, M., & Suganthan, P. N. (2022). Ensemble deep learning: A review. Engineering Applications of Artificial Intelligence, 115, 105151. https://doi.org/10.1016/j.engappai.2022.105151

840 Giaccio, B., Isaia, R., Fedele, F. G., Di Canzio, E., Hoffecker, J., Ronchitelli, A., ... & Popov, V. V. (2008). The Campanian Ignimbrite and Codola tephra layers: two temporal/stratigraphic markers for the Early Upper Palaeolithic in southern Italy and eastern Europe. Journal of Volcanology and Geothermal Research, 177(1), 208-226. https://doi.org/10.1016/j.jvolgeores.2007.10.007

Giaccio, B., Galli, P., Peronace, E., Arienzo, I., Nomade, S., Cavinato, G., Mancini, M., Messina, P., & Sottili, G. (2014).
845 A 560–440 ka tephra record from the Mercure Basin, southern Italy: volcanological and tephrostratigraphic implications. Journal of Quaternary Science, 29, 3, 232-248. https://doi.org/10.1002/jqs.2696

Giannetti, B. (2001). Origin of the calderas and evolution of Roccamonfina volcano (Roman Region, Italy). Journal of Volcanology and Geothermal Research, 106(3-4), 301-319. https://doi.org/10.1016/S0377-0273(00)00259-6

Granger, C. W., & Ramanathan, R. (1984). Improved methods of combining predictions. Journal of Predictioning, 3(2),
850 197-204.

Greenlee, D. D. (1987). Raster and vector processing for scanned linework. Photogrammetric Engineering and Remote Sensing, 53, 1383-1387.

Guidoboni, E., & Ciuccarelli, C. (2011). The Campi Flegrei caldera: historical revision and new data on seismic crises, bradyseisms, the Monte Nuovo eruption and ensuing earthquakes (twelfth century 1582 AD). Bulletin of volcanology,
855 73, 655-677. https://doi.org/10.1007/s00445-010-0430-3

Hofmann-Wellenhof, B., Lichtenegger, H., & Collins, J. (2001). Global positioning system: theory and practice. Springer-Verlag Wien GmbH. Vienna. https://doi.org/10.1007/978-3-7091-6199-9

Hsiao, C., & Wan, S. K. (2014). Is there an optimal prediction combination? Journal of Econometrics, 178, 294-309.

Ihlen, V. (2019) Landsat 8 Data Users Handbook. US Geological Survey, Sioux Falls, SD, USA

860 Isaia, R., D'Antonio, M., Dell'Erba, F., Di Vito, M., & Orsi, G. (2004). The Astroni volcano: the only example of closely spaced eruptions in the same vent area during the recent history of the Campi Flegrei caldera (Italy). Journal of Volcanology and Geothermal Research, 133(1-4), 171-192. https://doi.org/10.1016/S0377-0273(03)00397-4

Isaia, R., Marianelli, P., & Sbrana, A. (2009). Caldera unrest prior to intense volcanism in Campi Flegrei (Italy) at 4.0 ka BP: Implications for caldera dynamics and future eruptive scenarios. Geophysical Research Letters, 36(21).
865 https://doi.org/10.1029/2009GL040513

Jensen, J. R. (2015). Introductory Digital Image Processing: A Remote Sensing Perspective. Pearson Education.

Jenson, S. K., & Domingue, J. O. (1988). Extracting topographic structure from digital elevation data for geographic information system analysis. Photogrammetric Engineering and Remote Sensing, 54(11), 1593-1600.

Kienast-Brown, S., Libohova, Z., & Boettinger, J. (2017). Digital soil mapping, In Ditzler, C., Scheffe, K., & Monger, H.
870 C. (Eds.). Soil science division staff. Soil survey manual. USDA Handbook, pp. 295-354.

Krakiwsky, E.J., & Wells, D.E. (1971). Coordinate Systems In Geodesy. Geodesy and Geomatics Engineering, UNB, Lecture Notes, No. 16.

Lancaster, P., & Salkauskas, K. (1986). Curve and surface fitting: An introduction. Academic Press, London.

Li, J., Lu, X., Cheng, K., Liu, W., & Li, M. J. (2020). StepReg: Stepwise Regression Analysis. R package version 1.4.4,
875 https://CRAN.R-project.org/package=StepReg

Ligas, M., & Banasik, P. (2011). Conversion between Cartesian and geodetic coordinates on a rotational ellipsoid by solving a system of nonlinear equations. Geodesy and Cartography, 60(2), 145-159. https://doi.org/10.2478/v10277-012-0013-x

Lirer, L., Luongo, G., & Scandone, R. (1987). On the volcanological evolution of Campi Flegrei. Eos, Transactions
880 American Geophysical Union, 68(16), 226-234. https://doi.org/10.1029/EO068i016p00226

Liu, H., Harris, J., Sherlock, R., Behnia, P., Grunsky, E., Naghizadeh, M., ... & Hill, G. (2023). Mineral prospectivity mapping using machine learning techniques for gold exploration in the Larder Lake area, Ontario, Canada. Journal of Geochemical Exploration, 107279. https://doi.org/10.1016/j.gexplo.2023.107279

Lowe, D. J. (2011). Tephrochronology and its application: a review. Quaternary Geochronology, 6(2), 107-153. https://doi.org/10.1016/j.quageo.2010.08.003

Matano, F., De Chiara, G., Ferlisi, S., & Cascini, L. (2016). Thickness of pyroclastic cover beds: the case study of Mount Albino (Campania region, southern Italy). Journal of Maps, 12(sup1), 79-87. http://dx.doi.org/10.1080/17445647.2016.1158668

Matano, F., Ebrahimi, P., Angelino, A., & Grimaldi, G. M. (2023). Database of pyroclastic cover deposit thickness measurements (PT-Cam) in peri-volcanic areas of Campania (Italy) (1.0) [Data set]. Zenodo. https://doi.org/10.5281/zenodo.8399487

Mele, D., Dellino, P., Sulpizio, R., & Braia, G. (2011). A systematic investigation on the aerodynamics of ash particles. Journal of Volcanology and Geothermal Research, 203(1-2), 1-11. http://dx.doi.org/10.1016/j.jvolgeores.2011.04.004

Newbold, P., & Granger, C. W. (1974). Experience with predictioning univariate time series and the combination of predictions. Journal of the Royal Statistical Society: Series A (General), 137(2), 131-146.

Newhall, C. G., & Self, S. (1982). The volcanic explosivity index (VEI) an estimate of explosive magnitude for historical volcanism. Journal of Geophysical Research: Oceans, 87(C2), 1231-1238. https://doi.org/10.1029/JC087iC02p01231

Nowotarski, J., Raviv, E., Trück, S., & Weron, R. (2014). An empirical comparison of alternative schemes for combining electricity spot price predictions. Energy Economics, 46, 395-412. https://doi.org/10.1016/j.eneco.2014.07.014

Nti, I. K., Adekoya, A. F., & Weyori, B. A. (2020). A comprehensive evaluation of ensemble learning for stock-market prediction. Journal of Big Data, 7(1), 20. https://doi.org/10.1186/s40537-020-00299-5

Orsi, G., D'Antonio, M., de Vita, S., & Gallo, G. (1992). The Neapolitan Yellow Tuff, a large-magnitude trachytic phreatoplinian eruption: eruptive dynamics, magma withdrawal and caldera collapse. Journal of Volcanology and Geothermal Research, 53(1-4), 275-287. https://doi.org/10.1016/0377-0273(92)90086-S

Orsi, G., De Vita, S., & Di Vito, M. (1996). The restless, resurgent Campi Flegrei nested caldera (Italy): constraints on its evolution and configuration. Journal of Volcanology and Geothermal Research, 74(3-4), 179-214. https://doi.org/10.1016/S0377-0273(96)00063-7

Orsi, G., Di Vito, M. A., & Isaia, R. (2004). Volcanic hazard assessment at the restless Campi Flegrei caldera. Bulletin of Volcanology, 66, 514-530. https://doi.org/10.1007/s00445-003-0336-4

Pappalardo, L., Civetta, L., D'Antonio, M., Deino, A., Di Vito, M., Orsi, G., ... & Piochi, M. (1999). Chemical and Sr-isotopical evolution of the Phlegraean magmatic system before the Campanian Ignimbrite and the Neapolitan Yellow Tuff eruptions. Journal of Volcanology and Geothermal Research, 91(2-4), 141-166. https://doi.org/10.1016/S0377-0273(99)00033-5

Passariello, I., Lubritto, C., D'Onofrio, A., Guan, Y., & Terrasi, F. (2010). The Somma–Vesuvius complex and the Phlaegrean Fields caldera: new chronological data of several eruptions of the Copper–Middle Bronze Age period. Nuclear Instruments and Methods in Physics Research Section B: Beam Interactions with Materials and Atoms, 268(7-8), 1008-1012. https://doi.org/10.1016/j.nimb.2009.10.085

Patacca, E., Sartori, R., & Scandone, P. (1990). Tyrrhenian basin and Apenninic arcs: kinematic relations since late Tortonian times. Memorie della Società Geologica Italiana, 45, 425-451. Perrotta, A., & Scarpati, C. (2003). Volume partition between the plinian and co-ignimbrite air fall deposits of the Campanian Ignimbrite eruption. Mineralogy and Petrology, 79, 67-78. https://doi.org/10.1007/s00710-003-0002-8

Perrotta, A., Scarpati, C., Luongo, G., & Morra, V. (2006). The Campi Flegrei caldera boundary in the city of Naples. In Developments in Volcanology, Editor(s): B. De Vivo, Elsevier, Volume 9, 85-96, https://doi.org/10.1016/S1871-644X(06)80019-7

925  Piochi, M., Mastrolorenzo, G., & Pappalardo, L. (2005). Magma ascent and eruptive processes from textural and compositional features of Monte Nuovo pyroclastic products, Campi Flegrei, Italy. Bulletin of Volcanology, 67, 663-678. https://doi.org/10.1007/s00445-005-0410-1

Qi, J., Chehbouni, A., Huete, A. R., Kerr, Y. H., & Sorooshian, S. (1994). A modified soil adjusted vegetation index. Remote Sensing of Environment, 48(2), 119-126. https://doi.org/10.1016/0034-4257(94)90134-1

930  Qin, C., Zhu, A. X., Pei, T., Li, B., Zhou, C., & Yang, L. (2007). An adaptive approach to selecting a flow-partition exponent for a multiple-flow-direction algorithm. International Journal of Geographical Information Science, 21(4), 443-458. https://doi.org/10.1080/13658810601073240

Ribeiro, M. H. D. M., & dos Santos Coelho, L. (2020). Ensemble approach based on bagging, boosting and stacking for short-term prediction in agribusiness time series. Applied Soft Computing, 86, 105837.
935  https://doi.org/10.1016/j.asoc.2019.105837

Rolandi, G., Maraffi, S., Petrosino, P., & Lirer, L. (1993a). The Ottaviano eruption of Somma-Vesuvio (8000 y BP): a magmatic alternating fall and flow-forming eruption. Journal of Volcanology and Geothermal Research, 58(1-4), 43-65. https://doi.org/10.1016/0377-0273(93)90101-V

Rolandi, G., Mastrolorenzo, G., Barrella, A. M., & Borrelli, A. (1993b). The Avellino plinian eruption of Somma-
940  Vesuvius (3760 y.B.P.): the progressive evolution from magmatic to hydromagmatic style. Journal of Volcanology and Geothermal Research, 58(1-4), 67-88. https://doi.org/10.1016/0377-0273(93)90102-W

Rolandi, G., Munno, R., & Postiglione, I. (2004). The AD 472 eruption of the Somma volcano. Journal of Volcanology and Geothermal Research, 129(4), 291-319. https://doi.org/10.1016/S0377-0273(03)00279-8

Rolandi, G., Paone, A., Di Lascio, M., & Stefani, G. (2008). The 79 AD eruption of Somma: The relationship between
945  the date of the eruption and the southeast tephra dispersion. Journal of Volcanology and Geothermal Research, 169(1-2), 87-98. https://doi.org/10.1016/j.jvolgeores.2007.08.020

Rolandi, G., Petrosino, P., & Mc Geehin, J. (1998). The interplinian activity at Somma–Vesuvius in the last 3500 years. Journal of Volcanology and Geothermal Research, 82(1-4), 19-52. https://doi.org/10.1016/S0377-0273(97)00056-5

Rosi, M., & Sbrana, A. (1987). Phlegrean fields. Quaderni de La Ricerca Scientifica, 9(114).

950  Rosi, M., Sbrana, A., & Vezzoli, L. (1988). Correlazioni tefrostratigraphiche di alcuni livelli di Ischia, Procida e Campi Flegrei. Memorie della Societa Geologica Italiana, 41, 1015-1027.

Rosi, M., Vezzoli, L., Aleotti, P., & De Censi, M. (1996). Interaction between caldera collapse and eruptive dynamics during the Campanian Ignimbrite eruption, Phlegraean Fields, Italy. Bulletin of Volcanology, 57, 541-554. https://doi.org/10.1007/BF00304438

955  Rosi, M., Vezzoli, L., Castelmenzano, A., & Grieco, G. (1999). Plinian pumice fall deposit of the Campanian Ignimbrite eruption (Phlegraean Fields, Italy). Journal of Volcanology and Geothermal Research, 91(2-4), 179-198. https://doi.org/10.1016/S0377-0273(99)00035-9

Rouchon, V., Gillot, P. Y., Quidelleur, X., Chiesa, S., & Floris, B. (2008). Temporal evolution of the Roccamonfina volcanic complex (Pleistocene), Central Italy. Journal of Volcanology and Geothermal Research, 177(2), 500-514.
960  https://doi.org/10.1016/j.jvolgeores.2008.07.016

Saco, P. M., Willgoose, G. R., & Hancock, G. R. (2006). Spatial Organization of Soil Depths using a Landform Evolution Model/ NOVA. The University of Newcastle's Digital Repository: Newcastle.

Santacroce, R., & Sbrana, A. (2003). Carta geologica del Vesuvio. Scala 1:15,000. Progetto CARG. Sevizio Geologico Nazionale - Consiglio Nazionale delle Ricerche. Firenze: S.E.L.C.A.

965   Santacroce, R. (1987). Somma-Vesuvius. Quaderni de La Ricerca Scientifica, CNR Roma,114 (8), 251 pp.

Santacroce, R., Cioni, R., Marianelli, P., Sbrana, A., Sulpizio, R., Zanchetta, G., ... & Joron, J. L. (2008). Age and whole rock–glass compositions of proximal pyroclastics from the major explosive eruptions of Somma-Vesuvius: A review as a tool for distal tephrostratigraphy. Journal of Volcanology and Geothermal Research, 177(1), 1-18. https://doi.org/10.1016/j.jvolgeores.2008.06.009

970   Saulnier, G. M., Beven, K., & Obled, C. (1997). Including spatially variable effective soil depths in TOPMODEL. Journal of Hydrology, 202(1-4), 158-172. https://doi.org/10.1016/S0022-1694(97)00059-0

Sbrana, A., Cioni, R., Marianelli, P., Sulpizio, R., Andronico, D., & Pasquini, G. (2020). Volcanic evolution of the Somma-Vesuvius complex (Italy). Journal of Maps, 16(2), 137-147. https://doi.org/10.1080/17445647.2019.1706653

Scarpati, C., & Perrotta, A. (2016). Stratigraphy and physical parameters of the Plinian phase of the Campanian Ignimbrite

975   eruption. GSA Bulletin, 128(7-8), 1147-1159. https://doi.org/10.1130/B31331.1

Scarpati, C., Sparice, D., & Perrotta, A. (2014). A crystal concentration method for calculating ignimbrite volume from distal ash-fall deposits and a reappraisal of the magnitude of the Campanian Ignimbrite. Journal of Volcanology and Geothermal Research, 280, 67-75. https://doi.org/10.1016/j.jvolgeores.2014.05.009

Segoni, S., Martelloni, G., & Catani, F. (2013). Different methods to produce distributed soil thickness maps and their

980   impact on the reliability of shallow landslide modeling at catchment scale. In Margottini, C., Canuti, P., Sassa, K. (Eds). Landslide Science and Practice. Springer: Berlin; 127-133.

Sevink, J., van Bergen, M. J., van der Plicht, J., Feiken, H., Anastasia, C., & Huizinga, A. (2011). Robust date for the Bronze age Avellino eruption (Somma-Vesuvius): 3945±10 calBP (1995±10 calBC). Quaternary Science Reviews, 30(9-10), 1035-1046. https://doi.org/10.1016/j.quascirev.2011.02.001

985   Smith, V. C., Isaia, R., & Pearce, N. J. G. (2011). Tephrostratigraphy and glass compositions of post-15 kyr Campi Flegrei eruptions: implications for eruption history and chronostratigraphic markers. Quaternary Science Reviews, 30(25-26), 3638-3660. https://doi.org/10.1016/j.quascirev.2011.07.012

Smith, V. C., Isaia, R., Engwell, S. L., & Albert, P. G. (2016). Tephra dispersal during the Campanian Ignimbrite (Italy) eruption: implications for ultra-distal ash transport during the large caldera-forming eruption. Bulletin of Volcanology,

990   78, 1-15. https://doi.org/10.1007/s00445-016-1037-0

Sulpizio, R., Bonasia, R., Dellino, P., Mele, D., Di Vito, M. A., & La Volpe, L. (2010a). The Pomici di Avellino eruption of Somma–Vesuvius (3.9 ka BP). Part II: sedimentology and physical volcanology of pyroclastic density current deposits. Bulletin of Volcanology, 72, 559-577. https://doi.org/10.1007/s00445-009-0340-4

Sulpizio, R., Cioni, R., Di Vito, M. A., Mele, D., Bonasia, R., & Dellino, P. (2010b). The Pomici di Avellino eruption of

995   Somma-Vesuvius (3.9 ka BP). Part I: stratigraphy, compositional variability and eruptive dynamics. Bulletin of Volcanology, 72, 539-558. https://doi.org/10.1007/s00445-009-0339-x

Sulpizio, R., Mele, D., Dellino, P., & La Volpe, L. (2007). Deposits and physical properties of pyroclastic density currents during complex Subplinian eruptions: the AD 472 (Pollena) eruption of Somma-Vesuvius, Italy. Sedimentology, 54(3), 607-635. https://doi.org/10.1111/j.1365-3091.2006.00852.x

1000  Sulpizio, R., Mele, D., Dellino, P., & La Volpe, L. (2005). A complex, Subplinian-type eruption from low-viscosity, phonolitic to tephri-phonolitic magma: the AD 472 (Pollena) eruption of Somma-Vesuvius, Italy. Bulletin of Volcanology, 67, 743-767. https://doi.org/10.1007/s00445-005-0414-x

Tarboton, D. G., Bras, R. L., & Rodriguez-Iturbe, I. (1991). On the extraction of channel networks from digital elevation data. Hydrological Processes, 5(1), 81-100. https://doi.org/10.1002/hyp.3360050107

Tarquini, S., Isola, I., Favalli, M., & Battistini, A. (2007). TINITALY, a digital elevation model of Italy with a 10 m-cell size (Version 1.0) [Data set]. Istituto Nazionale di Geofisica e Vulcanologia (INGV). https://doi.org/10.13127/TINITALY/1.0

Taylor, J., & Tibshirani, R. J. (2015). Statistical learning and selective inference. Proceedings of the National Academy of Sciences, 112(25), 7629-7634. https://doi.org/10.1073/pnas.1507583112

Tesfa, T. K., Tarboton, D. G., Chandler, D. G., & McNamara, J. P. (2009). Modeling soil depth from topographic and land cover attributes. Water Resources Research, 45(10). 1-16. https://doi.org/10.1029/2008WR007474

Vitale, S., & Isaia, R. (2014). Fractures and faults in volcanic rocks (Campi Flegrei, Southern Italy): Insights into volcano tectonic processes. International Journal of Earth Sciences, 103(3), 801–819. https://doi.org/10.1007/s00531-013-0979-0

Wohletz, K., Orsi, G., & De Vita, S. (1995). Eruptive mechanisms of the Neapolitan Yellow Tuff interpreted from stratigraphic, chemical, and granulometric data. Journal of Volcanology and Geothermal Research, 67(4), 263-290. https://doi.org/10.1016/0377-0273(95)00002-C

Wong, K. K., Song, H., Witt, S. F., & Wu, D. C. (2007). Tourism predictioning: to combine or not to combine?. Tourism Management, 28(4), 1068-1078. https://doi.org/10.1016/j.tourman.2006.08.003

Wright, M. N., & Ziegler, A. (2017). ranger: A fast implementation of random forests for high dimensional data in C++ and R. Journal of Statistical Software, 77(1), 1–17. https://doi.org/10.18637/jss.v077.i01

Xiao, J., Shen, Y., Tateishi, R., & Bayaer, W. (2006). Development of topsoil grain size index for monitoring desertification in arid land using remote sensing. International Journal of Remote Sensing, 27(12), 2411-2422. https://doi.org/10.1080/01431160600554363

Yang, D. (2018). Spatial prediction using kriging ensemble. Solar Energy, 171, 977-982. https://doi.org/10.1016/j.solener.2018.06.105

Zevenbergen, L. W., & Thorne, C. R. (1987). Quantitative analysis of land surface topography. Earth Surface Processes and Landforms, 12(1), 47-56. https://doi.org/10.1002/esp.3290120107